NASA/TM—2010-216095

Effect of Microscopic Damage Events on Static and Ballistic Impact Strength of Triaxial Braid Composites

Justin D. Littell
ATK Space Systems, Hampton, Virginia

Wieslaw K. Binienda and William A. Arnold
The University of Akron, Akron, Ohio

Gary D. Roberts and Robert K. Goldberg
Glenn Research Center, Cleveland, Ohio

March 2010

NASA STI Program . . . in Profile

Since its founding, NASA has been dedicated to the advancement of aeronautics and space science. The NASA Scientific and Technical Information (STI) program plays a key part in helping NASA maintain this important role.

The NASA STI Program operates under the auspices of the Agency Chief Information Officer. It collects, organizes, provides for archiving, and disseminates NASA's STI. The NASA STI program provides access to the NASA Aeronautics and Space Database and its public interface, the NASA Technical Reports Server, thus providing one of the largest collections of aeronautical and space science STI in the world. Results are published in both non-NASA channels and by NASA in the NASA STI Report Series, which includes the following report types:

- TECHNICAL PUBLICATION. Reports of completed research or a major significant phase of research that present the results of NASA programs and include extensive data or theoretical analysis. Includes compilations of significant scientific and technical data and information deemed to be of continuing reference value. NASA counterpart of peer-reviewed formal professional papers but has less stringent limitations on manuscript length and extent of graphic presentations.

- TECHNICAL MEMORANDUM. Scientific and technical findings that are preliminary or of specialized interest, e.g., quick release reports, working papers, and bibliographies that contain minimal annotation. Does not contain extensive analysis.

- CONTRACTOR REPORT. Scientific and technical findings by NASA-sponsored contractors and grantees.

- CONFERENCE PUBLICATION. Collected papers from scientific and technical conferences, symposia, seminars, or other meetings sponsored or cosponsored by NASA.

- SPECIAL PUBLICATION. Scientific, technical, or historical information from NASA programs, projects, and missions, often concerned with subjects having substantial public interest.

- TECHNICAL TRANSLATION. English-language translations of foreign scientific and technical material pertinent to NASA's mission.

Specialized services also include creating custom thesauri, building customized databases, organizing and publishing research results.

For more information about the NASA STI program, see the following:

- Access the NASA STI program home page at *http://www.sti.nasa.gov*

- E-mail your question via the Internet to *help@ sti.nasa.gov*

- Fax your question to the NASA STI Help Desk at 443–757–5803

- Telephone the NASA STI Help Desk at 443–757–5802

- Write to:
  NASA Center for AeroSpace Information (CASI)
  7115 Standard Drive
  Hanover, MD 21076–1320

Effect of Microscopic Damage Events on Static and Ballistic Impact Strength of Triaxial Braid Composites

Justin D. Littell
ATK Space Systems, Hampton, Virginia

Wieslaw K. Binienda and William A. Arnold
The University of Akron, Akron, Ohio

Gary D. Roberts and Robert K. Goldberg
Glenn Research Center, Cleveland, Ohio

National Aeronautics and
Space Administration

Glenn Research Center
Cleveland, Ohio 44135

March 2010

Acknowledgments

Level of Review: This material has been technically reviewed by technical management.

Effect of Microscopic Damage Events on Static and Ballistic Impact Strength of Triaxial Braid Composites

Justin D. Littell
ATK Space Systems
Hampton, Virginia 23681

Wieslaw K. Binienda and William A. Arnold
The University of Akron
Akron, Ohio 44325

Gary D. Roberts and Robert K. Goldberg
National Aeronautics and Space Administration
Glenn Research Center
Cleveland, Ohio 44135

Abstract

The reliability of impact simulations for aircraft components made with triaxial-braided carbon-fiber composites is currently limited by inadequate material property data and lack of validated material models for analysis. Methods to characterize the material properties used in the analytical models from a systematically obtained set of test data are also lacking. A macroscopic finite element based analytical model to analyze the impact response of these materials has been developed. The stiffness and strength properties utilized in the material model are obtained from a set of quasi-static in-plane tension, compression and shear coupon level tests. Full-field optical strain measurement techniques are applied in the testing, and the results are used to help in characterizing the model. The unit cell of the braided composite is modeled as a series of shell elements, where each element is modeled as a laminated composite. The braided architecture can thus be approximated within the analytical model. The transient dynamic finite element code LS-DYNA is utilized to conduct the finite element simulations, and an internal LS-DYNA constitutive model is utilized in the analysis. Methods to obtain the stiffness and strength properties required by the constitutive model from the available test data are developed. Simulations of quasi-static coupon tests and impact tests of a represented braided composite are conducted. Overall, the developed method shows promise, but improvements that are needed in test and analysis methods for better predictive capability are examined.

Introduction

A wide range of materials, fiber architectures, and manufacturing methods are available to make carbon-fiber composite components for fixed wing aircraft and the engines that power these vehicles. For some potential new applications, the use of textile composites offers the opportunity to meet performance requirements at a cost that is comparable with current technology. A recent development is the use of composite materials in fan cases for jet engines. Approaches using triaxial braid preforms with various resin combinations have been developed for this application. To achieve airworthiness certification a full scale engine blade-out test must be performed to demonstrate that the fan containment system can contain a released fan blade and that the fan case can maintain sufficient structural integrity to survive the large dynamic loads imparted by the unbalanced rotor during spool down. Blade and case deformation during a fan blade-out event can usually be simulated with sufficient accuracy using commercial explicit finite element codes. Fragmentation of the fan blade and failure of the case can also be simulated for engines that utilize traditional metallic blade and case materials. The accuracy of the simulations currently achievable for metallic systems is the result of having an adequate material database and having a large

experience base for test/analysis correlation during development and certification of many engines that are currently in service. There is much less material data available and very limited experience with test/analysis correlation for fan containment systems that utilize composite fan cases. The ultimate goal of current research is to improve the blade-out simulation capability for composite fan cases to a level comparable to that achievable for metallic cases. The work presented in this paper is a first step toward that goal. In this paper, a computationally efficient method for representing the braid architecture in impact simulations is presented. An important objective in this work is to develop methods to apply the results from material characterization tests to obtain material property data in a form that is needed for the composite material models used in the analysis. Ballistic impact tests were performed on composite panels in a way that approximates the impact velocity, deformation mode, and strain energy density at failure for composite material in a fan case during blade-out. These impact test results are used for test/analysis correlations

There has been a significant amount of research conducted in the analysis and modeling of textile composites. The majority of the efforts have concentrated on various means to determine the effective mechanical properties of woven materials. Among the earliest attempts to model these materials were made by Chou and Ishikawa (Ref. 1). In their original mosaic model, the woven composite was approximated as a one-dimensional series of laminated cross-ply composites, and classical laminate theory in combination with iso-stress or iso-strain assumptions were applied to obtain the effective stiffness properties of the material. They later extended the model to account for the fiber undulations that are present in an actual woven material (Ref. 1). This approach was extended to two-dimensions by Naik and Shembekar (Ref. 2), in which a mixture of parallel and series assumptions were applied to obtain the effective properties of the material. To analyze more complicated fiber architectures, such as braided composites, researchers such as Pastore and Gowayed (Ref. 3) and Byun (Ref. 4) modeled the fibers as a series of rods at various angles, and utilized simple iso-strain assumptions to obtain the overall effective properties of the composite. More sophisticated analysis methods, such as those developed by Tanov and Tabiei (Ref. 5) and Bednarcyk (Ref. 6), used an approach where a representative unit cell of a woven composite was created, and then micromechanics-based approaches were applied to compute the effective properties and response of the material. In the context of applying these methods within a finite element model, elements are created with a homogenized set of material properties, and the appropriate analysis method is used to generate the effective properties and response of the woven material.

In all of the previously developed analytical methods, homogenized elements are used, in which the architecture of the textile material is not directly accounted for within a finite element model. However, for triaxially braided composites, experimental evidence has shown (Ref. 7) that when these materials are subject to impact, oftentimes the damage will propagate along the fiber directions. To simulate these damage patterns, the braid architecture should be directly simulated within the finite element model. To account for the fiber architecture in a computationally efficient manner, Cheng (Ref. 8) created a "Braided Through the Thickness" approach, where the braided composite is modeled as a series of layered shell elements, where each element is a laminated composite with the appropriate fiber layup. The effective stiffness and strength material properties of the equivalent unidirectional composite then were included as input data for the finite element analysis. In the method developed by Cheng, fiber and matrix properties were combined using simple micromechanics-based approaches to obtain the required effective properties. The model was developed within the context of LS-DYNA (Ref. 9), a commercially available transient dynamic finite element code which is commonly used within the aerospace industry. A continuum damage mechanics based composite constitutive model available within LS-DYNA was used as the material model.

In the work described in this paper, two major extensions to the approach developed by Cheng have been made. First of all, in actual braided composites, the layers of braid often do not directly sit on top of each other, but instead fiber nesting takes place. In this work, the way that the discretization of the braid has been adjusted to account for this phenomenon will be described. More significantly, in the previously developed methods, the effective unidirectional composite properties of the materials utilized in a braided composite either had to be measured experimentally or computed by using micromechanics techniques.

This approach requires an extensive additional experimental program, with tests on either the matrix constituent (for micromechanics approaches) or the equivalent unidirectional composites, besides tests on the braided composite, being required to obtain the needed data. These test programs can be quite complicated, with no guarantee that the experimental properties obtained are representative of the in-situ properties of the material. Furthermore, if micromechanics based approaches are directly applied within the analysis model, the computational cost can be increased significantly. In the approach to be described in this paper, the equivalent unidirectional properties of the composite can be extracted based on data obtained from coupon tests of the braided composite. In this manner, the in-situ properties are directly incorporated into the input for the material model, which also reduces the amount of testing that is required. Furthermore, without the need to incorporate micromechanics methods into the analysis through some sort of local-global approach, the computational efficiency of the simulations can be significantly increased. Alternatively, using an approach of this type can be useful as a tool to verify the more sophisticated analysis approaches.

Material Background

The composite materials that are currently of most interest for engine fan cases are made by resin infusion processes using two-dimensional triaxial braided preforms and 177 °C (350 °F) cure epoxy resins. Many fiber/matrix combinations have been investigated. This paper will focus on results obtained using TORAYCA T700S fiber (Toray Carbon Fibers America, Inc.) and CYCOM PR 520 matrix (Cytec Industries, Inc.). T700S is a high strength, standard modulus carbon fiber. The Toray fiber was a high strength, standard modulus fiber used in applications where tensile strength was needed. The fibers are known to behave as linear elastic material exhibiting an abrupt or brittle failure when the maximum failure strain and stress is reached. Table 1 shows the properties of the T700 fiber, as reported by Toray.

TABLE 1.—COMPOSITE FIBER PROPERTIES

	Tensile strength, MPa	Young's modulus, GPa	Failure strain, percent	Density, g/cm^3
Toray T700 fiber	4900	230	2.1	1.80

PR520 is a one part toughened resin specifically designed for the RTM process. Results obtained using the T700S/PR520 material system will be presented for the purpose of demonstrating issues related to test method development and implementation of test data in impact analysis. Some additional results will be presented using the same fiber and Hexcel's 3502 resin. Hexcel's 3502 resin is a general purpose thermoset resin with a cure temperature of 177 °C. Table 2 lists the mechanical properties of each resin, as reported by each manufacturer.

TABLE 2.—COMPOSITE RESIN PROPERTIES

	Tensile strength, MPa	Young's modulus, GPa	Density, g/cm^3
Cytec CYCOM PR520	82	4.0	1.256
Hexcel 3502	33	3.6	1.266

The two-dimensional triaxial braid preforms were made by A&P Technology, and composite panels were fabricated by resin transfer molding (RTM) at North Coast Composites. A 0/+60/–60 triaxial braid architecture was used. A picture of the preform and a representative unit cell are shown in Figure 1. A single unit cell is highlighted. A unit cell is the smallest repeating geometry that can represent the entire composite material as a whole. This unit cell will become important when developing the braided geometry for use in computer simulations, because the computer simulations will model repeating patterns of this single unit cell.

In Figure 1 the ±60° bias fibers are visible on the surface. Portions of the 0° axial fibers that lie below the ±60° bias fibers can be seen in the open spaces between the ±60° bias fibers. The 0° axial fibers were 24 k flattened tows while the ±60° bias fibers were 12 k flattened tows. Although larger fiber bundles
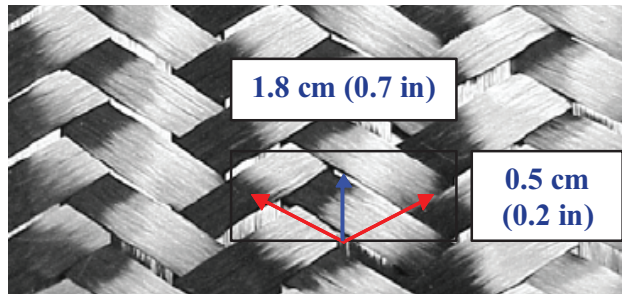
Figure 1.—Triaxial Braided Composite Fiber Layup with highlighted unit cell. The axial fiber direction is in blue and the bias fiber direction is in red.

were used in the axial direction, the fiber bundle spacing in the axial and bias directions were adjusted to give the same fiber volume in the axial and bias directions. This fiber architecture is quasi-isotropic in-plane, so the global in-plane stiffness is expected to be the same in all directions when the region of interest includes several unit cells of the braid material.

Composite panels were fabricated by placing six layers of the 0/+60/–60 braid preform into the RTM mold with the 0° fibers aligned in the same direction. Although the axial (0°) fibers in the various layers were aligned, the lateral position of the axial tows in the six layers was random. Resin was injected into the closed mold and cured according to processing conditions recommended by the resin manufacturer. Cured panel dimensions (after trimming) were 0.6096 m (2 ft) wide by 0.6096 m (2 ft) long by 0.3175 cm (0.125 in.) thick. Fiber volume of the cured composites was measured using the acid digestion technique. The T700S/PR520 composite had a fiber volume of 55.9±0.18 percent. The T700S/3502 composite had a fiber volume of 59.9±4.64 percent.

Experimental Methods

Standard test methods have been developed that rely on having a uniform deformation field in the gage section of the test specimen in order to accurately measure in-plane tension, compression, and shear properties. Results of tests on materials with a triaxial architecture like that of Figure 1 have indicated that modifications to standard test methods are needed because the large fiber bundle size and large unit cell size can result in nonuniform deformation within the gage section and within the unit cell. In addition, premature failure resulting from edge effects can result in failure modes for the coupon that cause artificially low strength measurements. To generate material property data needed for the development, characterization and validation of the analytical methods to be described later in this paper, tests on the triaxial braid composites were performed using standard methods for measuring properties in tension (Ref. 10), compression (Ref. 11), and shear (Refs. 12 and 13). However, as will be described briefly here and is covered in more detail in Roberts, et al. (Ref. 14), there are some deficiencies in the standard test methods which may affect the quality of the data. Specimens were tested in a hydraulically actuated, 220-kN (50-kip) test machine under displacement control with a displacement rate of 0.635 mm/min (0.025 in./min).

One difference from the standard methods was the use of digital image correlation methods to measure full-field strain instead of using strain gages or extensometers. A commercial image correlation system was used. Load measurements from the test rig were input to the image correlation system to generate stress-strain curves. The digital image correlation technique is similar to that described by Littell (Ref. 15). A brief summary is provided here. Two cameras are connected to a computer equipped with software capable of pattern recognition and calculation of position from stereo images. A calibration procedure is performed in which a series of images of known dimensions are placed in the intersecting field of view of the two cameras, and the location of the image is mapped by the software. This results in a calibrated volume of space that can be used for tracking displacement of test specimens under load. The test specimen is painted with a speckle pattern for optimum pattern recognition. A three-dimensional map of the specimen surface is obtained before the specimen is loaded. The specimen is then loaded, and the
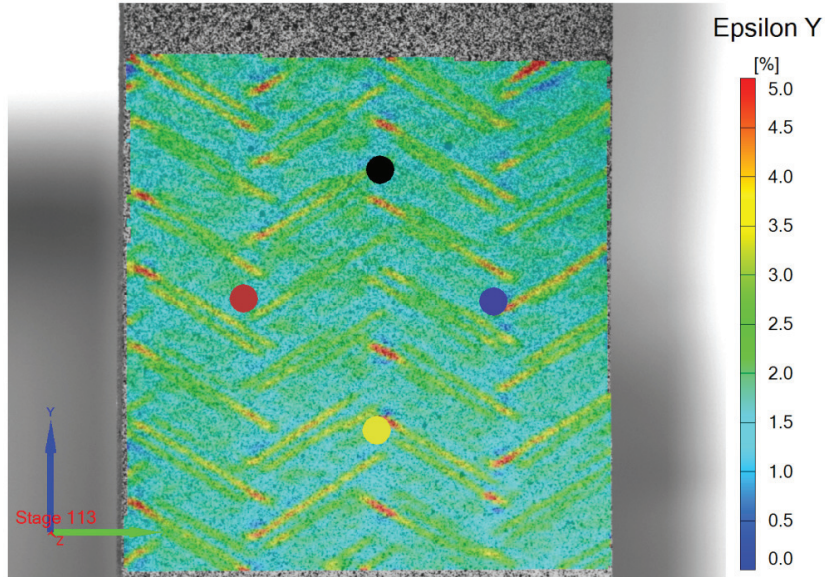
Figure 2.—Typical axial strain field in an axial tensile test. Colored dots indicate the points used for global strain calculations in the axial and transverse directions.

pattern recognition software is able to track the three-dimensional displacement of any point which remains in the initial field of view. Strain is then calculated from surface displacements measured at specified time intervals during a test. Stress-strain curves are calculated from the synchronized load and strain measurements.

Figure 2 shows an example of the axial strain field measured at one specific time step during an axial tensile test.

The field of view in Figure 2 captures the entire 3.578 cm (1.409 in.) specimen width and approximately 5.08 cm (2 in.) of the specimen height. The strain field in Figure 2 is nonuniform and shows high strain regions within the braid architecture that can become sites for local damage. An average strain can be calculated by averaging the nonuniform strain within a particular field of view, or by tracking the location of specific points. A potential problem with the averaging approach is that the calculated strain can be affected by unrealistically high strain values and possible loss of pattern recognition at local damage sites. To avoid this complication, global strain was measured by tracking specific points that are separated by a distance that is large compared to the size of the local damage. The locations of these points, which are approximately 1.905 cm (0.75 in.) apart, are indicated in Figure 2. The two points aligned along the specimen vertical axis are used to calculate axial strain, and the two points aligned along the specimen horizontal axis are used to calculate transverse strain. Global strains are calculated by dividing the relative displacement between the two points in the loaded condition by their original separation in the unloaded condition. This is later referred to as an "optical strain gage". Tests were performed to measure tension compression and shear properties in axial and transverse directions. In the axial tests, the axial braid fibers are aligned along the load direction. In the transverse tests the axial braid fibers are aligned perpendicular to the load direction. The full-field strain measurements were used during all of these tests to examine the uniformity of the strain field and to attempt to identify local deformation and damage within the braid unit cell.

Compression Test Results

Compression tests were performed according to methods described in ASTM D-3410 (Ref. 11). Test specimens were 91 cm (6.0 in.) long by 3.58 cm (1.41 in.) wide. These dimensions allowed for a long gripped region with a short 2.54 cm (1.00 in.) gage section as specified by the standard test method. The
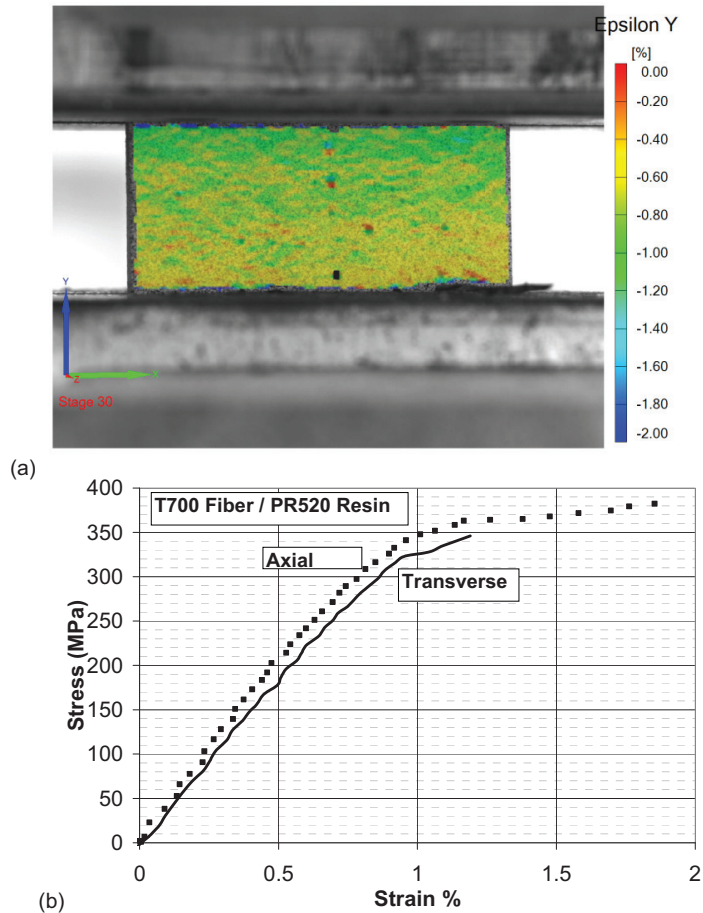
Figure 3.—Results of typical compression tests for the T700S/PR520 material system. (a) Axial compression test specimen showing a uniform axial strain field; (b) Axial and transverse compression stress-strain curves.

width was selected to include at least two unit cells. For an axial test, the width includes two unit cells and the length of the gage section includes five unit cells. For a transverse test, the width includes 7 unit cells, but the length of the gage section includes less than one and a half unit cells. At least two unit cells in the gage length would be preferred, but a longer gage length is not desirable because it increases the possibility of buckling.

   A representative full-field strain map for a T700S/PR520 axial compression specimen is shown in Figure 3(a). The deformation in Figure 3(a) is homogeneous with no perceptible effect of the braid architecture. The deformation observed in transverse compression tests was also homogeneous. The failure mode for a T700S/PR520 axial compression specimen was found to occur in the middle of the gage section, and there is no evidence of premature failure resulting from edge effects. Typical axial and transverse compression stress-strain curves for T700S/PR520 are shown in Figure 3(b). Only two tests were performed for each orientation to determine average material properties because of limited material availability. Additional testing is planned when materials become available. Compression test results are shown in Table 3 for the two material systems reported in this work.

TABLE 3.—COMPRESSION PROPERTIES

Material	Axial			Transverse		
Fiber-resin	Strength, MPa	Modulus, GPa	Failure strain, percent	Strength, MPa	Modulus, GPa	Failure strain, percent
T700-PR520	378	41.9	1.80	346	39.0	1.10
T700-3502	321	41.8	0.86	243	41.1	0.61

Shear Test Results

For the shear testing, a test specimen design based on the ASTM D-7078 "V-Notched Rail Shear Method" (Ref. 13) and which is described in detail in Roberts, et al. (Ref. 14) was employed. Advantages of the D-7078 method over the classical Iopescu Shear Test are discussed in (Ref. 14). For the triaxial braid architecture investigated in this work it was found that some edge damage can occur along the 45° edge between the notch and the clamps. To overcome this limitation, a modified "H" specimen geometry was developed and used for this work. Figure 4 shows a failed T700S/PR520 specimen held by one of the specimen grips after a test. Figure 5 shows the horizontal strain and shear strain distributions in the gage area of an "H" specimen immediately before failure.
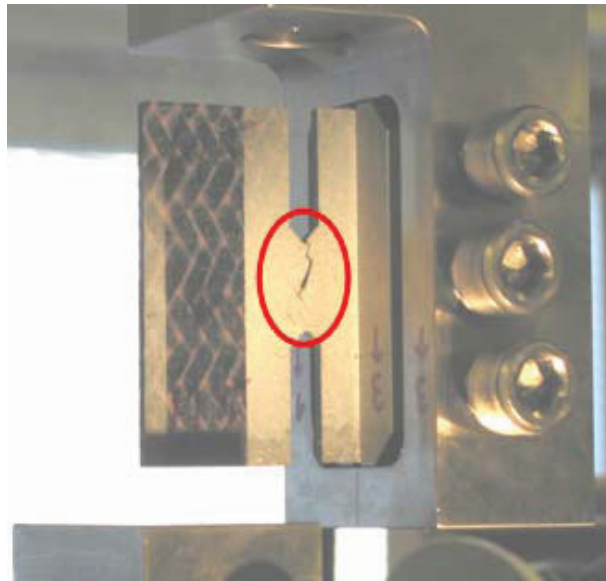

Figure 4.—A modified "H" specimen after failure with the left grip removed to view the crack.
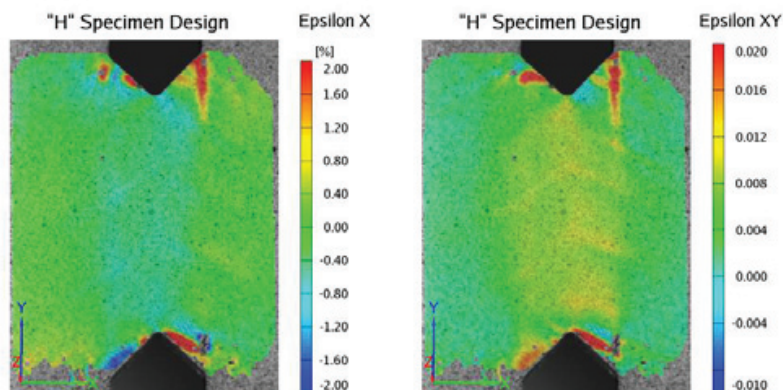

Figure 5.—Horizontal strain (left) and shear strain (right) measured using the modified "H" specimen for the ASTM D-7078 V-Notched Rail Shear Method using a T700S/PR520 specimen.
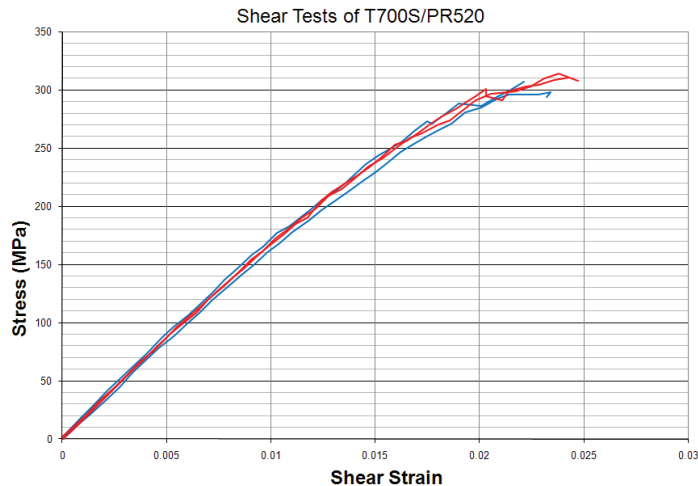
Figure 6.—Shear stress versus shear strain curves for the
T700S/PR520 material system.

In Figure 5, the shear deformation is located mostly within the gage area. The width of the deformation region is similar to the notch width of 0.7 cm (0.28 in.). In Figure 5 the axial braid fibers are horizontal, and there is about one unit cell within the width of the deformed area. A test specimen with vertical orientation of axial braid fibers would have about one third of a unit cell within the width of the deformed region. The effect of unit cell size relative to the size of the deformation area needs to be further examined in order to establish the validity of the test method for determining global shear properties. The regions of red and dark blue are damaged areas resulting from termination of fiber bundles at specimen edges. Modifications of the notch size and shape are being considered to reduce these edge failures. The strain near the center of the gage area was calculated over an area that is approximately 0.3 by 0.3 mm. Different median and average techniques were used and shown to have very little effect on the measured value, though further investigation is needed to develop a standard method for analyzing and extracting the desired values from the full-field strain results. Sample shear stress versus shear strain curves for the T700S/PR520 system are shown in Figure 6.

Table 4 shows average shear properties for the T700S/PR520 and T700S/3502 material systems. Shear modulus was measured as the slope of the stress-strain curve between 0 and 0.2 percent strain. Strength and failure strain were taken at the last measured point before failure, which was defined as a sudden significant (usually greater than 25 percent) decrease in load (most specimens) or the point at which the curve shows no further load increase. Error limits in Table 2 represent one standard deviation.

TABLE 4.—SHEAR PROPERTIES

Material	Shear	
	Strength, MPa	Modulus, GPa
T700-PR520	307±6.8	17.5±0.3
T700-3502	224±30	16.9±0.6

Tensile Test Results

The strain fields observed in the compression and shear tests presented above were nearly homogeneous. The effect of the braid architecture on the uniformity of the strain field within the gage area and within the unit cell was small, and in many cases not detected at all. In contrast, the strain field in tensile test specimens showed effects of the braid architecture within the entire gage area and within the unit cell. The pattern of the ±60° bias fibers on the surface of the specimen is clearly visible in Figure 2. The nonuniform strain field has been investigated for various material systems and discussed in detail in (Ref. 14). Some results from (Ref. 14) are reviewed in this section.
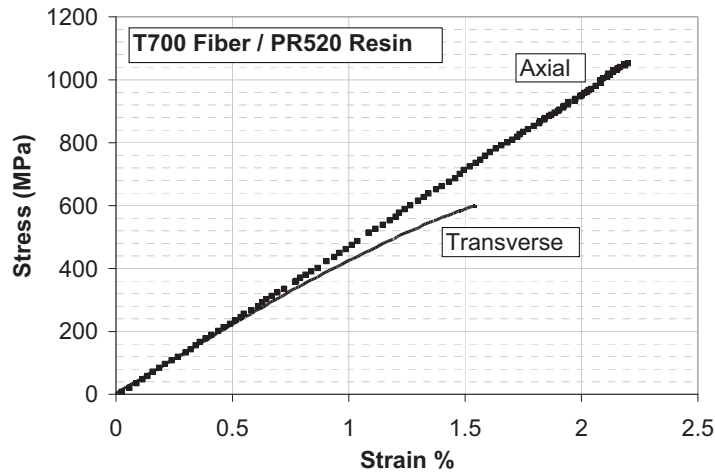
Figure 7.—Global stress versus global strain for T700S/PR520 axial and transverse tensile tests.

Straight sided tensile test specimens were prepared in accordance with ASTM D-3039 (Ref. 13). 30.48 cm (12 in.) length by 3.578 cm (1.409 in.) width dimensions were used for the tensile tests. These dimensions were chosen so that the width contained at least two unit cells and the length conformed to the ASTM D-3039 length to width ratios. Typical axial and transverse tensile test results for T700S/PR520 specimens are shown in Figure 7.

Five measurements were performed for each material system. Average measured properties are shown in Table 5 for both of the material systems considered in this report. Error limits in Table 5 represent one standard deviation.

TABLE 5.—TENSILE PROPERTIES

Material	Axial			Transverse		
Fiber-resin	Strength, MPa	Modulus, GPa	Failure, strain, percent	Strength, MPa	Modulus, GPa	Failure strain, percent
T700-PR520	1046±34	47.6±1.0	2.16±0.09	599±3.3	42.0±2.3	1.69±0.19
T700-3502	608±56	47.2±2.0	1.51±0.14	336±11	40.6±4.1	1.00±0.15

Premature failure near fiber bundles that terminate at free edges can influence the shape of the stress-strain curve and the measured failure strain. A large amount of edge damage was observed in both axial and transverse tensile tests. In an axial tensile test the axial braid fibers lie along the specimen axis and are gripped on both ends during a test.

Since these axial braid fibers carry most of the load, the reduction in strength caused by edge damage is small for the axial tensile test. The axial tensile stress-strain curve shown in Figure 6 is therefore linear until failure. The edge damage has a larger effect on the measured strength for the transverse tensile test because all of the axial braid fibers are perpendicular to the applied load. There is no continuous load path between the grips through fibers because all axial and bias fiber bundles terminate at a free edge. The edge damage most likely contributes to the nonlinearity of the transverse tensile stress-strain curve in Figure 6 and also most likely contributes to the reduced transverse failure stress compared to the axial failure stress. The axial strain field in a T700S/PR520 transverse tensile specimen loaded close to failure is shown in Figure 8(a). Global stress versus local strain is shown in Figure 8(b) for the four locations indicated by points in Figure 8(a).
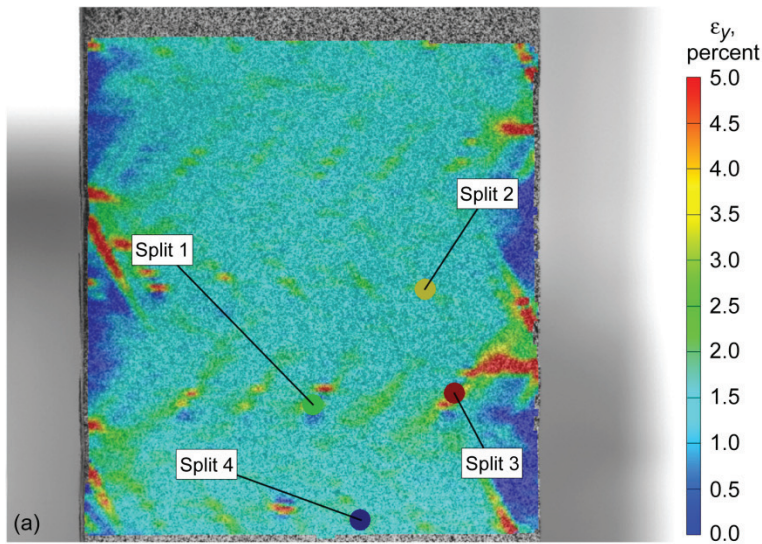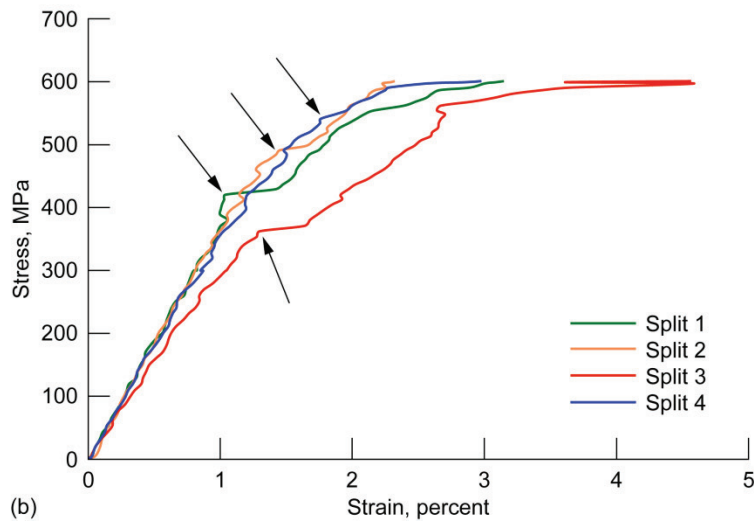
Figure 8.—Transverse tensile test results for T700S/PR520. (a) Full-field strain data. (b) Global stress versus local strain plot.

The dark blue triangular regions near the edges of the specimen in Figure 8(a) are regions of low strain that are not carrying load because of edge damage. In Figure 8(a) the edge-damaged region is about 10 percent of the specimen width. Since the damaged region does not carry load, the stress in the undamaged region is about 10 percent higher than the stress that is calculated based on the initial cross-sectional area of the specimen. The transverse stress-strain curve in Figure 7 is therefore most likely not an accurate representation of the transverse tensile properties. However, data is currently not available that eliminates these difficulties; therefore, the data as presented will be used to characterize the analytical model described below, with the realization that the actual characterized values used may need to be adjusted as improved data is obtained. In addition to the edge damage, localized damage is visible as small horizontal lines throughout the specimen in Figure 8(a). These local regions of high strain occur as a result of splitting in the subsurface axial braid fiber bundles, which lie in a horizontal direction in Figure 8(a). The locations of the first four splits that occur are indicated by colored dots in Figure 8(a). The local strain in the regions of these fiber bundle splits can be measured for each time step in the test. Figure 8(b) shows the global stress versus local strain curves for the four split locations. The global stress

versus local strain curves in Figure 8(b) are similar to the transverse global stress versus global strain curve in Figure 6 up to about 1 percent strain. The curves in Figure 8(b) show an abrupt increase in local strain at the locations indicated by arrows. These abrupt increases are associated with splitting of the subsurface axial-braid fiber bundles. The strain at which the abrupt increase occurs can be considered to be the in-situ transverse fiber bundle failure strain for the axial braid fiber bundles. The global stress at which the abrupt increase in strain occurs can be assumed to approximate the transverse bundle failure stress. The mean value of strain at transverse failure was approximately 1.4 percent, with values ranging from 1.0 to 1.8 percent for the T700 fiber/PR520 resin material system. The global stress in which the transverse failures began to occur was approximately 350 MPa. These parameters will be utilized in the characterization of the material model described below. These are useful material properties for analysis if it is assumed that the failure strain measured on the surface is the same as the failure strain for interior plies. Some support for this assumption was found through microscopic examination of the interior of specimens which had been loaded to strains lower than the failure strain. Edge view images of specimens that were cut and polished indicated that the extent of fiber bundle splitting is similar for all plies.

Analytical Methods

Background and Overview

As discussed in the Introduction section, classical methods to analyze braided (and woven) composites involved the determination of the effective properties of the material. These effective properties can then be utilized as the input data to a finite element code. The architecture of these materials is not explicitly modeled. Instead, the material is modeled as an orthotropic material with a set of smeared, homogenized properties. A simulation of an impact test on a flat plate with homogenized material properties representative of a typical triaxially braided composite is shown in Figure 9. In this simulation, failure initiated at the center of the panel and cracks then propagated equally in the vertical and horizontal directions. The deflection of the panel up to the point of failure correlated well with experiments; however the onset of damage, and the crack pattern could not be simulated. The penetration threshold for a specific material could be simulated by adjusting input properties or numerical parameters within the code. However, there was no systematic way to set the material properties and model parameters such that the penetration threshold for a range of different materials could be simulated. Because homogenized material properties were used in the analysis the crack pattern in Figure 9 was determined by the panel geometry. Experimental results for panels made from many different material systems indicated that cracks most often follow one of the braid fiber directions (Ref. 14).
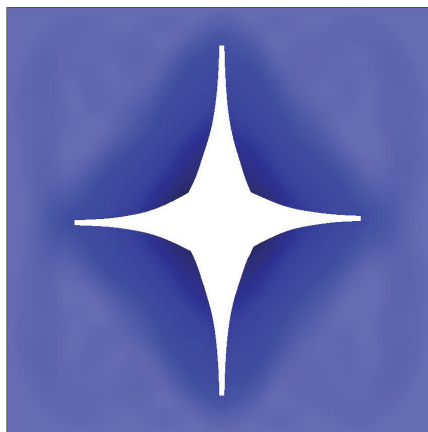

Figure 9.—Impact simulation using homogenous material properties showing horizontal and vertical cracks.
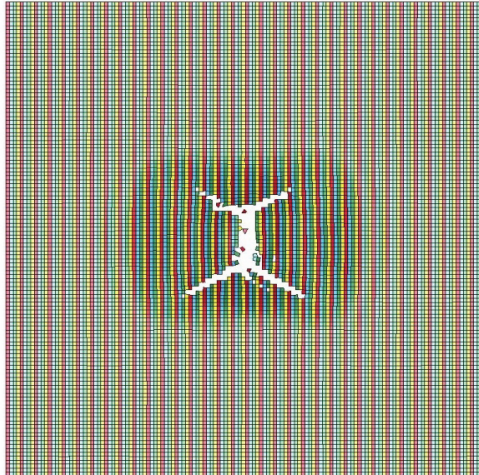
Figure 10.—Impact simulation using braided
through the thickness model showing
cracking pattern along bias fibers.

Cheng (Ref. 8) conducted a simulation of an impact test on the same material using the "Braided Through the Thickness" model, in which the braid is discretized into a series of parallel laminated composites using a method to be described below. In this simulation, as shown in Figure 10, failure initiates at the center of the panel. A crack first grows for a short distance along the direction of the 0° fibers then turns to propagate along the ±60° fiber directions. This behavior is close to that observed in experiments with some material systems. However, the model was not able to simulate the wide range of crack patterns observed experimentally. Correlations with the measured penetration threshold could be made by adjusting material properties and other parameters used in the analysis, but prediction of experimental results was not possible. The methods described in the remainder of this report build on the approach developed by Cheng. An approach for simulating a multilayer braided composite is presented, and a systematic method for utilizing experimentally measured material properties from coupon level tests is described.

Shell Element Representation of Braid Unit Cell

A finite element model of a unit cell of the braided composite is generated. A unit cell of a composite is the smallest unit of the composite for which the behavior of the unit can be assumed to be representative of the behavior of the composite as a whole. The unit cell defined for a single layer of the braided composite is identified in Figure 1. To model an entire structure, the unit cell mesh is replicated in a repeating pattern throughout the structure. For this work, the transient dynamic finite element code LS-DYNA (Ref. 9) was utilized. LS-DYNA was used due to its ability to simulate impact events.

A schematic of the braided composite unit cell is shown in Figure 11. In the schematic, –60° fibers are green, 0° fibers are blue or yellow and +60° fibers are red. For this work, the unit cell is subdivided into four parallel subcells, as shown in the figure. For the analysis model, each subcell is approximated to be a laminated composite, with fiber layups determined based on the braid geometry and unidirectional fiber tows stacked through the thickness. Subcell A is modeled as a [+60/0/–60] composite (bottom layer listed first). Subcell B is modeled as a [–60/+60] composite, subcell C is modeled as a [–60/0/+60] composite, and subcell D is modeled as a [+60/–60] composite.

-60	+60	+60	-60
0		0	
+60	-60	-60	+60
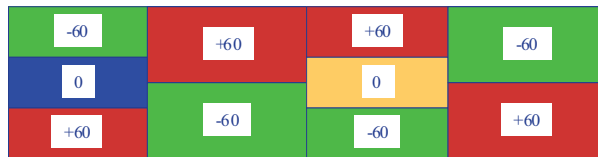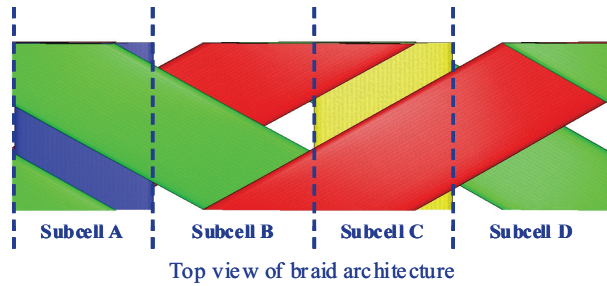
Edge view of shell elements representing the braid architecture

Figure 11.—Schematic of the triaxial braid unit cell showing discretization into four subcells.
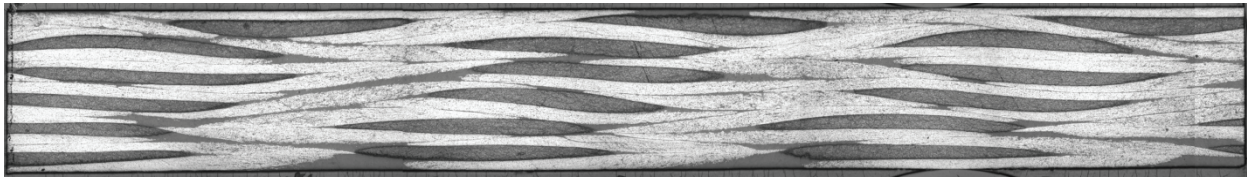

Figure 12.—Cross sectional cut demonstrating fiber tow shifting.

The actual braided composites examined in this study had six layers of braided fibers. The axial (0°) fibers in each layer were aligned, but the lateral position of axial fibers in each layer was random. As a result, axial fibers in the various layers are not located directly on top of each other. Instead, the axial fiber location in each layer is shifted in a random way relative to the location of axial fiber in the layers above and below. Figure 12 shows a sectional cut of an sample unit cell which represents an example of fiber shifting through the six layers of braided fibers. The black areas are the axial fibers, oriented perpendicular to the page, while the lighter areas represent the locations of the various +60 and –60° bias fibers. The gray areas represent resin rich pockets.

In generating the finite element model for the full six layer composite, this behavior was approximated by shifting each layer of fibers by one subcell to the left in the full model. A schematic of the full finite element model is shown in Figure 13, where subcell A is pink, subcell B is blue, subcell C is green and subcell D is yellow. The fiber shifting can be observed in this schematic. For example, in the top layer subcell D is the rightmost subcell. In the second layer subcell D is the second from the right subcell, and so on.

Accounting for the fiber shifting in the finite element model has other advantages. First of all, each subcell has 15 layers of fibers, which allows each layer to be given a constant thickness. The differences in sizes between the 24 k axial tows and 12 k bias tows was accounted for in the finite element model by weighting the axial layers twice the amount of the bias layers. Related to this, in actuality the +60 and –60 plies in subcells B and D in the one layer model would have a lower fiber volume ratio than the 0, +60, and –60 plies in subcells A and C, assuming that each subcell has a constant thickness. By incorporating the fiber shifting, the overall fiber volume ratio within each subcell is constant. Also, with this fiber layup, each subcell is a balanced composite, which eliminates the shear coupling terms within the stiffness matrix, which is useful for the backing out of the equivalent unidirectional properties to be described later. Finally, by incorporating the fiber shifting within the finite element model, each subcell will have 0°, 60°, and –60° fibers. In the original configuration, subcells B and D would have no 0° fibers, which might lead to them being overly weak in the axial direction.

Unit Cell

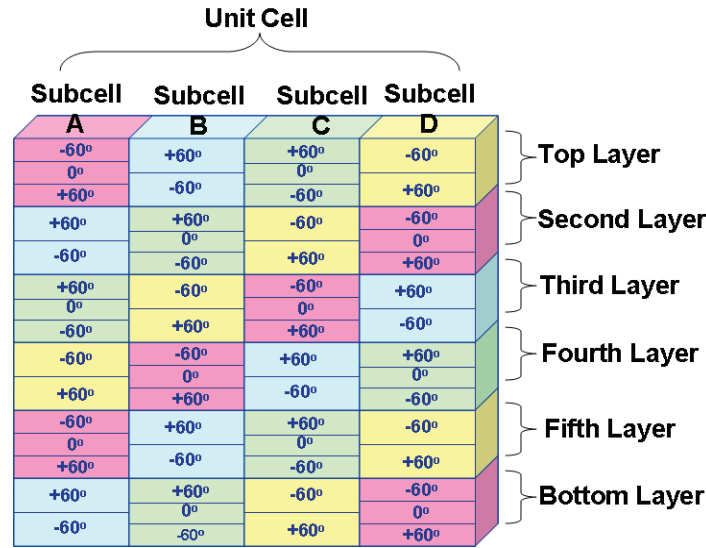| Subcell A	Subcell B	Subcell C	Subcell D	
$-60°$ / $0°$	$+60°$	$+60°$ / $0°$	$-60°$	Top Layer
$+60°$	$-60°$	$-60°$	$+60°$	
$+60°$	$+60°$ / $0°$	$-60°$	$-60°$ / $0°$	Second Layer
$-60°$	$-60°$	$+60°$	$+60°$	
$+60°$ / $0°$	$-60°$	$-60°$ / $0°$	$+60°$	Third Layer
$-60°$	$+60°$	$+60°$	$-60°$	
$-60°$	$-60°$ / $0°$	$+60°$	$+60°$ / $0°$	Fourth Layer
$+60°$	$+60°$	$-60°$	$-60°$	
$-60°$ / $0°$	$+60°$	$+60°$ / $0°$	$-60°$	Fifth Layer
$+60°$	$-60°$	$-60°$	$+60°$	
$+60°$	$+60°$ / $0°$	$-60°$	$-60°$ / $0°$	Bottom Layer
$-60°$	$-60°$	$+60°$	$+60°$	

Figure 13.—Schematic of subcell discretization of six layer triaxial braided composite.

Each of the subcells contained their own individual properties in the LS-DYNA model and was modeled as an individual shell element. Therefore, a unit cell consists of four shell elements. All of the subcells were modeled using shell elements since the length and width of the composite structures being examined were much greater than the thickness. Embedded within each shell element were parameters such as the total composite thickness, the number of composite layers through the thickness and also the relative weight (corresponding to the tow size) of each composite layer. The section parameters also contained information about the fiber orientation (0°, +60° or –60°) of each layer.

Determination of Material Properties

Unidirectional Stiffness Property Determination

The material model that is used for these analyses is a continuum damage mechanics based model for unidirectional composites, based on a theory developed by Matzenmiller, et al. (Ref. 16), that is implemented in LS-DYNA. In LS-DYNA, this model is referred to as *MAT_LAMINATED_ COMPOSITE_FABRIC and is labeled Material 58. For this material model, the required input stiffness parameters include the unidirectional ply level axial modulus (E_{11}), the transverse modulus (E_{22}), the in-plane shear modulus (G_{12}), and the in-plane Poisson's ratio (v_{21}). The unidirectional ply level strength data that is required includes the axial tensile and axial compressive failure stress and failure strain, the transverse tensile and transverse compressive failure stress and failure strain, and the in-plane shear failure stress and failure strain. The stiffness values are used by the material model to simulate the initial linear portion of the composite response. The ply level strength and ultimate strain values are used to determine the nonlinear portion of the material response, and to determine how the damage parameters used as internal variables within the material model evolve over the loading cycle. Furthermore, the user is allowed to specify a "stress limiting factor" in the longitudinal and/or transverse directions. If the value of the "stress limiting factor" is set to zero, the failure stress value is assumed to occur at the specified failure strain, and the material model then "connects the dots" (including enforcing any required material nonlinearity) in order to create the best-fit stress strain curve which accounts for the specified stiffness and strength values. If the "stress limiting factor" is set to one, the stress-strain curve of the composite is assumed to increase linearly until the maximum strength value is reached. At that point, the material is assumed to act as if it was a perfectly plastic material, with the strain in the specified direction increasing with no increase in stress until such point as the specified strain level is reached, at which point material failure is assumed to occur.
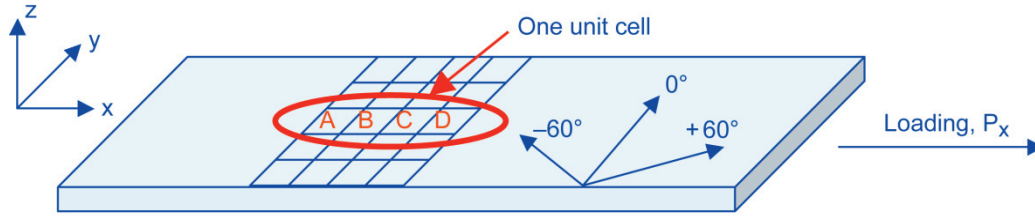
Figure 14.—Transverse tension test schematic.

The properties required by the model described above are the properties of the lamina (individual fiber bundles plus a portion of the surrounding resin material). A fundamental problem in the analysis of textile composites is that the lamina properties are not known and cannot be directly measured. Attempts can be made to fabricate unidirectional laminates using the same fiber tows that are used to make the preform. This approach is often not easy to accomplish, and the properties of the unidirectional lamina could be different from the properties of the fiber tows within the textile composite because of processing differences. For these reasons, a method was chosen that utilizes an approach based on micromechanics principles to calculate the lamina properties from experimental data obtained on the braided composite. Although there are also some limitations using this approach, the experimental requirements are simplified and the calculated lamina properties represent the in-situ properties of fiber bundles within the braided composite. The experimental methods described earlier in this paper provide the full set of data needed for the model, including guidance on how to specify the stress limiting factors mentioned earlier.

For both the stiffness and strength properties, test data from coupon tests on the braided composite were utilized to back out the equivalent unidirectional composite properties. To back out the stiffness properties, first the geometry of a coupon level transverse tensile test was considered, where the axial (0°) fibers are oriented perpendicular to the applied load, P_x. A schematic of a test of this type is shown in Figure 14. In this figure, the four subcells of the unit cell are oriented parallel to the applied load.

To relate the applied loads to the composite strains, the constitutive equations associated with classical laminate theory (Reference 17 being just one of many examples where this theory is discussed) were applied. Note that these equations use a load per unit length, so the applied load (P_x and P_y) was divided by the width of the coupon to get a load per unit length, N_x and N_y. Mathematically stated, the equations can be written as follows:

$$\begin{bmatrix} [N] \\ [M] \end{bmatrix} = \begin{bmatrix} [A] & [B] \\ [B] & [D] \end{bmatrix} \begin{bmatrix} [\varepsilon] \\ [\kappa] \end{bmatrix} \tag{1}$$

where the N matrix is a 3x1 matrix and represents the applied load in the x, y, and xy (shear) directions, the M matrix is a 3x1 matrix and represents the applied moments in the x, y, and xy direction, the A matrix is a 3x3 matrix and relates the in-plane 3x1 strain matrix (ε) to the applied load, the B matrix is a 3x3 matrix and couples the in-plane strain matrix to the applied moments or couples the bending strain 3x1 matrix (κ) to the applied load, and the D matrix is a 3x3 matrix.

Several assumptions were applied in the model development. The applied load was assumed to be equally divided between all of the braided layers, and between each of the unit cells along the width of the composite specimen. Therefore, the applied load could be related to the N_x term in Equation (1) by using the following relation:

$$N_x = \frac{P_x}{\left(\# \text{Layers}^* \# \text{Unit Cells}^* \text{Width} \right)} \tag{2}$$

where the P_x term is defined in Figure 14. This load represents the axial load in a single layer of the braided composite.

Furthermore, by assuming that the common assumptions of classical laminate theory were valid for each of the subcells, the axial and transverse strains for each subcell were assumed to be constant throughout the thickness of the subcell, and the strains measured on the outer surface of the composite by the use of the optical strain measurement techniques were assumed to be the strains throughout each of the layers of the subcell. Therefore, only the single layer unit cell (Fig. 11) was utilized in the analysis model. Each subcell was assumed to have a uniform fiber volume ratio to simplify the analysis, even though subcells B and D most likely have a lower fiber volume fraction than subcells A and C. Furthermore, each subcell was assumed to have a homogenized average strain (i.e., the strain between subcells could vary, but the strain within a subcell was assumed to be constant). Only in-plane loadings were considered, which resulted in the D matrix in Equation (1) not being utilized. In-plane normal-shear couplings were neglected (since the full six layer subcells were approximated as balanced composites), so the A_{16} and A_{26} components of the A matrix from Equation (1) were set equal to zero. Furthermore, even though the composite layups were antisymmetric, tension-bending coupling was neglected in order to simplify the analysis, which would result in the B matrix in Equation (1) being set equal to zero. This approximation was validated by the fact that no out-of-plane bending was observed in the testing of the braided composites as in-plane strains were applied. Furthermore, on a global level the full six layer braided composite could be viewed as approximately symmetric, which would result in the B matrix being equal to zero. The above assumptions can be applied to rewrite the constitutive equation for each subcell, such as is shown below for subcell A

$$
\begin{bmatrix} N_x^A \\ N_y^A \\ N_{xy}^A \end{bmatrix} = \begin{bmatrix} A_{11}{}^A & A_{12}{}^A & 0 \\ A_{12}{}^A & A_{22}{}^A & 0 \\ 0 & 0 & A_{66}{}^A \end{bmatrix} \begin{bmatrix} \varepsilon_x^A \\ \varepsilon_y^A \\ \varepsilon_{xy}^A \end{bmatrix}
\tag{3}
$$

where the superscript A represents the subcell name and the subscripts represent the directions. Similar equations for the remaining subcells could be written. The matrix equation in Equation (3) can be expanded to explicitly determine N_x, N_y, and N_{xy} in terms of the subcell strains for subcell A. Similar expressions can be derived for subcells B, C, and D. Since no shear loads were applied in this case, the shear load and shear strains were assumed to be zero.

Since subcells A and C both had the same layers of 0° fibers, layers of 60° fibers and layers of –60° fibers, and noting the various assumptions that were applied only subcell A was examined, since the two subcells would have an identical response. Similarly, since subcells B and D had the same number of 60° and –60° layers, only subcell B was examined.

For the transverse loading condition and the specified geometry, the applied load in each subcell in the loading direction was assumed to be equal (iso-stress type of assumption), which can be expressed as follows

$$
N_x^A = N_x^B = N_x^C = N_x^D = N_x
\tag{4}
$$

The volume average of the applied loads perpendicular to the loading direction in each of the subcells was assumed to be zero since there was no applied load in that direction, which can be expressed as follows

$$
V_f^A * N_y^A + V_f^B * N_y^B + V_f^C * N_y^C + V_f^D * N_y^D = 0
\tag{5}
$$

where V_f represented the volume fraction of each subcell as compared to the volume of the entire unit cell, and not the fiber volume fraction of the as-fabricated composite. Note that since subcell C was assumed to

be equivalent to subcell A and subcell D was assumed to be equivalent to subcell B Equation (4) can be rewritten as follows

$$2V_f^A N_y^A + 2V_f^B N_y^B = 0 \tag{6}$$

The constitutive equations and the various assumptions can be combined to back out the equivalent unidirectional properties of the braided composite by using the following procedure. First, the A matrix terms are written in terms of Q-bar, the transformed stiffness terms for a unidirectional ply in the structural axis system and the ply thickness in the manner of classical laminate theory as follows

$$A_{ij} = \sum_k \overline{Q}_{ij} t_k \tag{7}$$

where the sum is taken over the layers k and t_k is the thickness of the kth layer. For subcell A, the expansion can be written as follows

$$A_{11}^A = \overline{Q}_{11}^{60\,deg} * t + \overline{Q}_{11}^{0\,deg} * t + \overline{Q}_{11}^{-60\,deg} * t$$
$$A_{12}^A = \overline{Q}_{12}^{60\,deg} * t + \overline{Q}_{12}^{0\,deg} * t + \overline{Q}_{12}^{-60\,deg} * t$$
$$A_{22}^A = \overline{Q}_{22}^{60\,deg} * t + \overline{Q}_{22}^{0\,deg} * t + \overline{Q}_{22}^{-60\,deg} * t$$

$$\tag{8}$$

and in a similar manner the expansion for subcell B can be written

$$A_{11}^B = \overline{Q}_{11}^{-60\,deg} * t + \overline{Q}_{11}^{+60\,deg} * t$$
$$A_{12}^B = \overline{Q}_{12}^{-60\,deg} * t + \overline{Q}_{12}^{+60\,deg} * t \tag{9}$$
$$A_{22}^B = \overline{Q}_{22}^{-60\,deg} * t + \overline{Q}_{22}^{+60\,deg} * t$$

Note that Q-bar terms for the 0° fiber were not present in subcell B because 0° fibers were not present in subcell B. The Q-bar terms can then be decomposed into their representative Q terms, which represented the stiffness for a unidirectional ply layer in the material axis system for the axial, transverse and shear directions. Note that for subcell A the ply thickness t was equal to the overall layer thickness divided by three, since the equivalent laminated composite for subcell A had three plies. For subcell B, the ply thickness t was set equal to the overall layer thickness divided by two, since subcell B only had two plies in its equivalent laminated composite. Applying the classical stiffness matrix transformation equations, the structural axis stiffness terms can be written in terms of the material axis system stiffness terms as follows

$$\overline{Q}_{11} = m^4 * Q_{11} + n^4 * Q_{22} + 2 * n^2 * m^2 * Q_{12} + 4 * m^2 * n^2 * Q_{66}$$
$$\overline{Q}_{12} = m^2 * n^2 * Q_{11} + m^2 * n^2 * Q_{22} + (m^4 + n^4) * Q_{12} - 4 * m^2 * n^2 * Q_{66} \tag{10}$$
$$\overline{Q}_{22} = n^4 * Q_{11} + m^4 * Q_{22} + 2 * n^2 * m^2 * Q_{12} + 4 * m^2 * n^2 * Q_{66}$$

where m represents the cosine of the braid angle and n represents the sine of the braid angle. Equation (10) can be substituted into Equations (8) and (9) using the appropriate values for m and n based on the fiber angle.

Expanding Equation (3) in N_x and N_y for subcells A and B, and applying the assumptions in Equations (4) and (6) in Equations (8), (9), and (10) results in a set of 5 equations relating N_x and N_y for subcells A and B to the subcell strains. N_x is considered to be a known value from the transverse tension coupon test. The subcell level strains were also assumed to be known values. For a stress value from the initial linear portion of the stress strain curve the corresponding optical strain measurements occurring at that stress value were plotted and examined (Fig. 15). From the strain measurement map of the entire composite, a unit cell was identified, and subcells composing the unit cell were further identified. Within each subcell, the average axial and transverse strains within the subcell were determined by using the concept of a "digital strain gage", where the relative displacement of two points at opposite edges of the subcell were determined and divided by their original separation to obtain the strain. In this way the strain variation within the subcell was smeared out. To account for the large strain variation within the composite specimen, strain values were determined from multiple subcells (and unit cells) within the gage section and averaged. Furthermore, global stress (and corresponding subcell strain) values were determined from several locations in the linear portion of the transverse stress-strain curves, with their values being applied to the equations. The ability to consider the subcell strains as known values is new to this work and only possible due to the use of the optical strain measurement system.
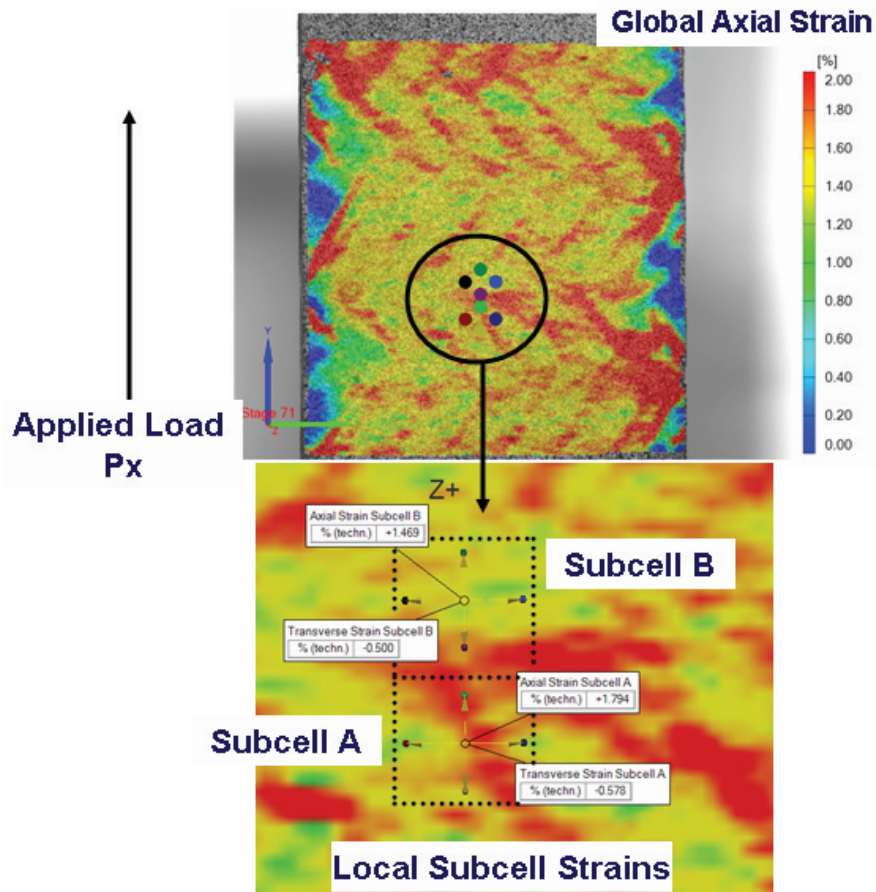

Figure 15.—Optical strain map of local subcell strains used to determine average subcell strains for determination of unidirectional composite stiffness properties.
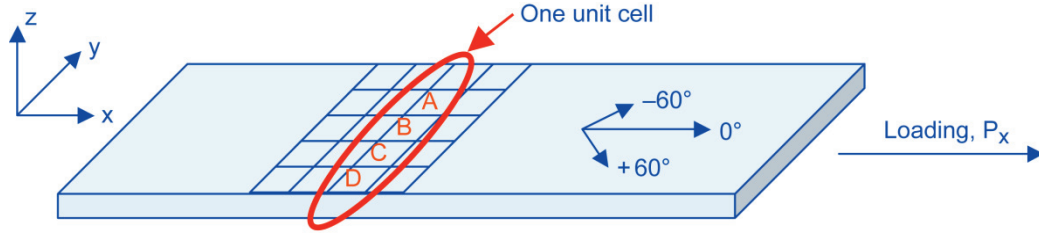
Figure 16.—Axial tension test schematic.

For the above equations, the unknowns include the subcell loads perpendicular to the loading direction, N_y^a, N_y^b, and the material axis system stiffness matrix values Q_{11}, Q_{12}, Q_{22}, and Q_{66}. Since there are six unknown values and only 5 equations available for finding the unknown variables, an additional equation must be developed. This equation was found from the modeling of an axial tensile test using the same ASTM 3039 specimen geometries. Figure 16 shows a representation of an axial tensile test, in which the axial (0°) fibers were oriented along the direction of loading, and the four subcells are oriented parallel to the direction of loading.

An important point to note for the discussion that follows is that the composite is once again assumed to be loaded in the "x" direction. That means that in terms of the unit cell orientation the axis orientation was switched 90° from the transverse loading case. In other words, what was considered to by the y direction previously is now the x direction, and vice versa. This change in axis orientation in relation to the equations presented above will be discussed below. For the axial testing case, the application of the iso-stress assumptions had to be modified due to the change in the test geometry. To generate the required additional equation, from the axial tension case only one of the uniform stress assumptions needed to be applied for the model development. For the case of axial tension, the unit cell is loaded along the x direction in Figure 16, which corresponds to the y direction in Figure 14 and Equations (1) to (10). Using the coordinate orientation of Figure 14, since the unit cell is being pulled in the y direction, the effective force in the x direction must be equal to zero. The force in the x direction in each of the subcells was also assumed to be equal. Expressed as equations, these assumptions translate to

$$N_x^A = N_x^B = N_x^C = N_x^D = 0 \tag{11}$$

The subcell constitutive equation (Eq. (3)) is expanded for the x direction (including the assumption stated in Equation (11)) only for subcells A and B to obtain the needed equation

$$N_x^A = 0 = A_{11}^{A}* \varepsilon_x^A + A_{12}^{A}* \varepsilon_y^A \tag{12}$$

$$N_x^B = 0 = A_{11}^{B}* \varepsilon_x^B + A_{12}^{B}* \varepsilon_y^B \tag{13}$$

where the subcell strains were again assumed to be known values and determined from optical strain data obtained during axial tension tests using the procedures described above.

Either Equation (12) or (13) could be used along with Equation (3) and Equations (8) to (10) to determine the six required variables (Q_{11}, Q_{12}, Q_{22}, Q_{66}, and N_y^a, N_y^b for the transverse tensile test). Between Equations (12) and (13), the equation that is not used for material characterization could be used to verify the accuracy of the determined parameters.

Since the ultimate goal was to find the unidirectional ply material properties required for the material model, the Q stiffness matrix terms were rewritten in terms of engineering material properties as follows

$$Q_{11} = \frac{E_{11}}{1 - v_{12}*v_{21}} \tag{14}$$

$$Q_{22} = \frac{E_{22}}{1 - v_{12} * v_{21}} \tag{15}$$

$$Q_{12} = \frac{v_{21} * E_{11}}{1 - v_{12} * v_{21}} \tag{16}$$

$$Q_{66} = G_{12} \tag{17}$$

where the unidirectional ply level axial modulus (E_{11}), transverse modulus (E_{22}), in plane shear modulus (G_{12}), and in plane Poisson Ratios (v_{12} and v_{21}) were the unknown variables. The classical reciprocal relationship provides an additional needed equation

$$\frac{E_{11}}{v_{12}} = \frac{E_{22}}{v_{21}} \tag{18}$$

Knowing the Q_{ij} from above and using Equations (14) to (18), E_{11}, E_{22}, G_{12}, v_{12}, and v_{21} can be found. These values are the effective unidirectional engineering properties of the composite ply at each integration point in the finite element model.

By using the measured subcell strains and values of load from the test data as the inputs into the material model, representative material properties can be found. Because the values of strain and load are measured from fabricated composite coupons, the model's effective unidirectional ply level properties implicitly include at least to some extent features such as the interface effects between the fibers and the matrix. Therefore, the material model represents the in-situ behavior of the composite and includes many of the local mechanisms present in the fabricated composite materials, but utilizes them in a macromechanical fashion.

Unidirectional Lamina Failure Property Development

The unidirectional strength values were also determined from the results of coupon tests on the braided material. The unidirectional strength parameters required by the continuum damage mechanics model utilized in this study include the parameters summarized in Table 6.

TABLE 6.—FAILURE VALUES NEEDED IN FINITE ELEMENT MATERIAL MODEL

Parameter	Description
E11T	Strain at longitudinal tensile strength
E11C	Strain at longitudinal compressive strength
E22T	Strain at transverse tensile strength
E22C	Strain at transverse compressive strength
GMS	Strain at in-plane shear strength
XT	Longitudinal tensile strength
XC	Longitudinal compressive strength
YT	Transverse tensile strength
YC	Transverse compressive strength
SC	Shear strength

The assumption was made that in an axial tensile test the load was primarily carried by the axial fibers, with the bias fibers making relatively small contributions. As a result, the axial failure stress and axial failure strain observed for the braided composite were assumed to be equal to the equivalent ply

level unidirectional axial failure stress and axial failure strain. This introduces a small error into the material property calculations that can be corrected in future work.

The strain field measured during axial compression tests was nearly uniform throughout the gage section with little effect of the braid architecture (Fig. 3(a)). The compressive strains in the axial fibers were therefore assumed to be equal to the global compressive strains in the composite. The compressive stress in the axial fibers was assumed to be equal to the global compressive stress. Therefore, the unidirectional compressive failure stress and failure strain were set equal to the measured global compressive failure stress and failure strain. Even though the compressive stress-strain curves had a significant amount of nonlinearity (Fig. 3(b)) near the end of the loading curve, and almost resembled a "perfectly plastic" response, the "stress limiting factor" was still set to zero. This parameter could lead to an underprediction of the compressive response at strains less than the failure strain.

To determine the equivalent transverse compressive failure stress and failure strain, once again the observation was made that during a transverse compression test, the compressive strains were relatively uniform throughout the gage section, indicating that the compressive strain (and by extension the compressive stress) for the axial fibers were equal to the compressive stress and strain for the braided composite. Therefore, once again the equivalent unidirectional transverse compressive failure stress and failure strain were set equal to the transverse compressive failure stress and failure strain for the braided composite. It is recognized that a more detailed analysis of the actual stress within the transverse fiber bundle will be needed for future refinement of the model.

To determine the equivalent transverse tensile failure stress of the unidirectional composite, the transverse tensile test data from the braided composites could not be used directly since in a transverse tension test, unlike in an axial tension test, the bias fibers significantly contribute to the global response of the composite. The lowest global transverse stress at which fiber splitting occurred (Fig. 8) was used as the transverse failure stress for the unidirectional composite. This assumption was made since the fiber bundle split was considered to be a result of matrix cracking, causing the fiber bundles to split in their transverse direction, which was assumed to represent a transverse failure of the unidirectional composite layer. Again, it is recognized that a more detailed analysis of the actual stress within the transverse fiber bundle is needed. The transverse failure strain, however, was assumed to be equal to the global transverse failure strain of the composite. In a braided composite the fiber bundles are constrained by adjacent fiber bundles, so multiple fiber bundles need to split within a braided layer before complete failure of the composite occurs.

To account for this behavior, the "stress limiting factor" in the transverse direction was set equal to one. This allowed the material to act as if it were a perfectly plastic material after the onset of fiber bundle splitting. Setting this parameter to 1 made each individual layer for each of the subcells in the model behave in an elastic-plastic manner in the transverse direction. In the elastic region, the fiber bundles carried load until they reached their ultimate stress value, and split. The response then became perfectly plastic. The plastic region represented the region in which each layer could not carry any more load and simulated the loading on the layer after a fiber bundle split occurred in the composite test. It allowed for the overall composite specimen to still carry load, even though individual fiber bundles could not. This meant that even though some of the individual fiber bundles failed, the overall specimen stress versus strain material response continued to grow until the final global transverse strain was reached. For a single layer, this behavior is shown schematically in Figure 17.

Figure 8(a) shows the full field strain measurement on a representative transverse coupon, and Figure 8(b) shows the local fiber bundle strain versus global coupon stress from a transverse tension test. The transverse tensile failure stress for the unidirectional layer was identified as the lowest global stress where a fiber split occurred, which in the case of Figure 8(b) was "split 3". The material response curve of the localized area around a fiber bundle split was not used after the fiber bundle split because of distortions in the optical strain measurements caused by the split. Accordingly, the local strain data
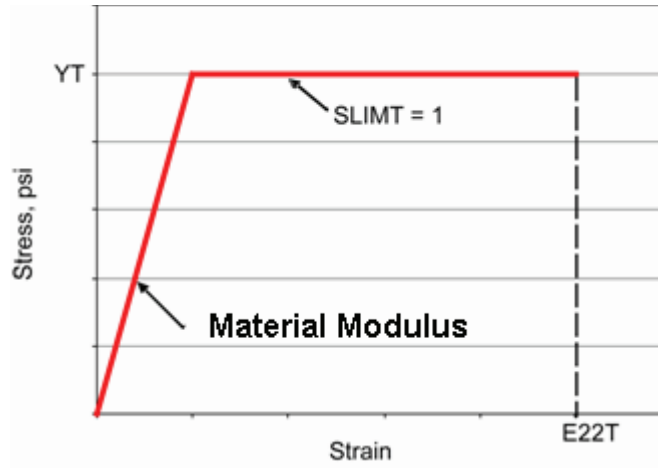
Figure 17.—Elastic-plastic material response parameters in the material model.
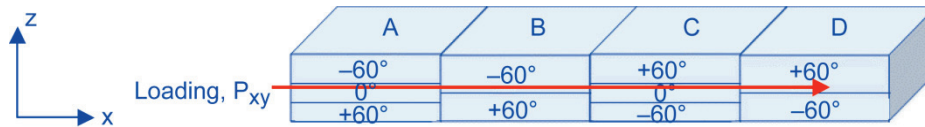

Figure 18.—Schematic of shear test specimen test setup.

obtained in the regions after the fiber split occurred was not used. Therefore, the global response data needed to be used to obtain the transverse failure strain. The overall composite failure strain in the test specimen was representative of a composite coupon failure from the accumulated damage created by the fiber bundle split propagations.

To compute the shear failure stress and the shear failure strain, the assumption was made that under pure shear loading, the shear stress and shear strain in every layer in all of the subcells was equal to the global shear stress and shear strain. Therefore, the equivalent unidirectional shear strength and shear failure strain was assumed to be equal to the shear failure stress and shear failure strain measured for the composite. A schematic of the shear test demonstrating this assumption is shown in Figure 18.

Simulation Results

Quasi-Static Tension

To demonstrate and verify the developed analytical methodology, a series of simulations were conducted. First, the quasi-static axial and transverse tensile tests on the T700/PR520 and the T700/3502 materials were simulated. The sample finite element meshes are shown in Figure 19. The finite element model for the axial tension test was 20.32 cm long, 3.56 cm wide, and had 369 nodes and 320 shell elements. The model for the transverse tensile test was 30.48 cm long, 3.56 cm wide, and had 522 nodes and 476 elements.

The fixed end of the model was constrained in all three displacement and rotation directions. The loading was an applied displacement applied at the rate of 0.0635 cm/sec, which was consistent with the test conditions. Each subcell was modeled as a shell element. In the figure, the red elements represent subcell A, the blue elements represent subcell B, the green elements represent subcell C and the yellow elements represent subcell D. Each subcell is modeled using an individual shell element. This allows the braid architecture to be explicitly modeled within the finite element mesh. The unit cell orientations for both of the modeling conditions are highlighted for reference. In the axial test simulation the unit cell is oriented perpendicular to the direction of the applied load. In the transverse test simulation the unit cell is oriented parallel to the direction of the applied load.
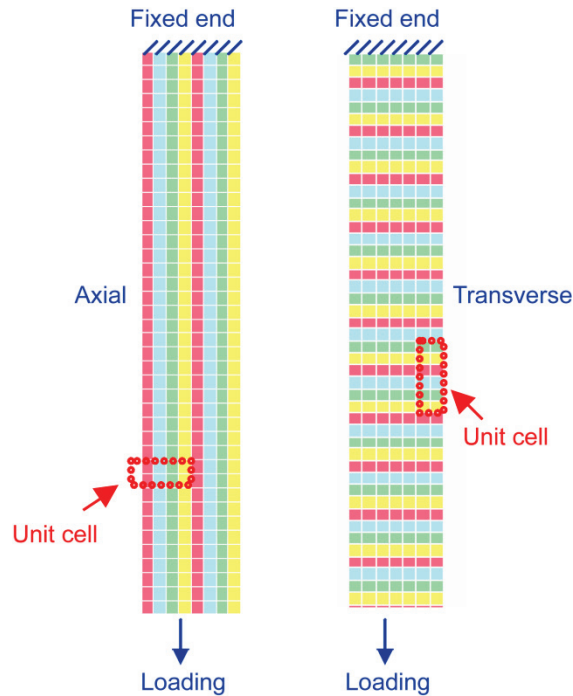
Figure 19.—Finite element models of axial tension (left) and transverse tension (right) tests.

TABLE 7.—MATERIAL PROPERTY VALUES USED FOR THE QUASI-STATIC COUPON SIMULATIONS

Material	T700–PR520	T700–3502
Material parameter name, LS-DYNA name	Value, unit	Value, unit
Axial Modulus, EA	51.37, GPa	51.37 GPa
Transverse Modulus, EB	25.03, GPa	25.03 GPa
In Plane Shear Modulus, GAB	18.96, GPa	18.96, GPa
In Plane Poisson Ratio, PRBA	0.071	0.071
Axial Tensile Failure Strain, E11T	0.0216	0.0151
Axial Compressive Failure Strain, E11C	0.018	0.01
Transverse Tensile Failure Strain, E22T	0.0168	0.01
Transverse Compressive Failure Strain, E22C	0.011	0.0068
In Plane Shear Failure Strain, GMS	0.024	0.02
Axial Tensile Stress at Failure, XT	1044.59, MPa	607.45, MPa
Axial Compressive Stress at Failure, XC	377.09, MPa	363.37, MPa
Transverse Tensile Stress at Failure, YT	361.99, MPa	68.95, MPa
Transverse Compressive Stress at Failure, YC	344.75, MPa	243.39, MPa
In Plane Shear Stress at Failure, SC	307.31, MPa	224.09, MPa
Stress Limiting Parameter for Axial Tension, SLIMT1	0	0
Stress Limiting Parameter for Transverse Tension, SLIMT2	1	1
Stress Limiting Parameter for Axial Compression, SLIMC1	0	0
Stress Limiting Parameter for Transverse Compression, SLIMC2	0	0
Stress Limiting Parameter for Shear, SLIMS	0	0

Tensile stress versus strain curves were generated for the T700/PR520 and the T700/3502 materials in both the axial and transverse directions. The material properties that were used for the analysis were determined using the methods described above and are shown in Table 7. In the simulations, material failure was deemed to occur when all of the elements in a row failed. The element failure occurred nearly simultaneously in the simulations, leading to a fairly abrupt ultimate failure.
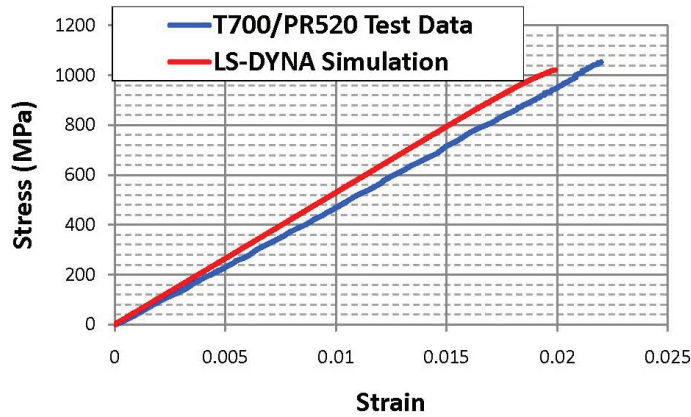
Figure 20.—Test versus simulation for T700 fiber/PR520 resin
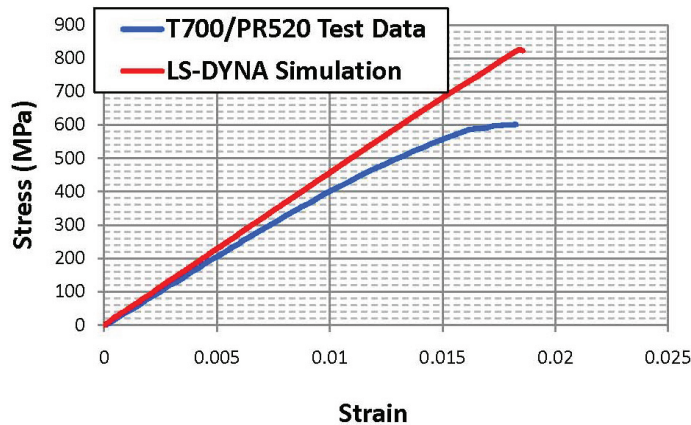axial tension material response.

Figure 21.—Test versus simulation for T700 fiber/PR520 resin
transverse tension material response.

Stress versus strain results were extracted from the simulations and compared to a representative test. The stresses versus strain results from the test were extracted from the optical measurement system. Axial tensile results for the T700/PR520 material are shown in Figure 20, and transverse tensile results for this material are shown in Figure 21. Table 8 shows a comparison between the experimental and computed moduli and strength for the axial tensile tests, and Table 9 shows a similar comparison for the transverse tensile tests. Note the numbers for the test data in the tables presented represent an average and one standard deviation for the tests conducted.

TABLE 8.—COMPARISONS BETWEEN T700 FIBER/PR520 RESIN TEST
AND LS-DYNA AXIAL TENSION DATA

	Axial tension modulus, GPa	Axial tension strength, MPa
Test	46.89±1.1	1048.04±33.79
LS–DYNA	52.88	1021.90
Error, percent	11	3

TABLE 9.—COMPARISONS BETWEEN T700 FIBER/PR520 RESIN TEST
AND LS-DYNA TRANSVERSE TENSION DATA

	Transverse tension modulus, GPa	Transverse tension strength, MPa
Test	42.75±1.6	599.18±2.96
LS–DYNA	45.90	822.17
Error, percent	7	27

For the case of axial tension loading, both the computed modulus and strength correlated well to the experimentally obtained values. The nearly linear nature of the axial tension stress-strain response was also captured by the simulations. The slight underprediction of the axial strength could be due to the fact that in the simulations all of the subcells in the gage section failed simultaneously, where in reality the failure of the fiber tows may be much more gradual due to the statistical nature of the fiber strength, and the fact that each fiber tow has many fibers.

For the transverse behavior, the computed modulus correlated well with the experimental value, but the simulated response was much more linear, with a significantly higher failure strength, than was observed in the experimental results. For both the experimental and simulated results, the transverse modulus was somewhat lower than the axial modulus, which should not be the case for a quasi-isotropic material. However, this discrepancy is most likely due to the fact, as discussed above, that the test geometry used for the transverse tensile test was not truly representative of the material response due to the fact that the bias fibers were not properly constrained. The cause of the discrepancy in failure strength is also most likely related to the test geometry used for the experiments. As mentioned above, the fact that the bias fibers were not properly constrained in the experiments most likely led to an artificial weakness in the experimental results, as the bias fibers could not properly contribute to the load resistance of the composite. Furthermore, the edge damage observed in the experimental tests could contribute strongly to the nonlinearity observed in the experiments. Due to the nature of the way in which the braid architecture was discretized and simulated in the analytical model, with the fiber tows not being modeled in a continuous manner, these local effects could not be captured in the simulations as each subcell in a sense is an independent laminated composite. As a result, the simulated results from the transverse tension test in all likelihood were more representative of the response that would be observed if the response was measured at a location far away from where edge effects would be significant. Therefore, the fact that the transverse tension response of the material was linear, like the axial tension response, with a transverse failure stress only slightly lower than the axial failure stress, is most likely actually more representative of the response of the material as utilized in an engineering structure.

There are two more features of the analytical method which probably need to be examined in more detail in order to improve the quality of the simulations. In the nested six layer braid model as used in the simulations, each subcell has the same number of 0, +60 and –60 layers, only arranged in different orders. Since all normal-shear and axial-bending coupling is neglected in the analysis (or, as in the case of the normal-shear coupling, falls out naturally due to the balanced laminate assumption), each subcell is essentially the same composite, thus eliminating any spatial variation in the material response, which could affect the predictions. Therefore, in the future the coupon level simulations will be repeated where the different layers of braid are assumed to stack evenly on top of each other. On a related point, as mentioned above within a single layer each of the subcells are assumed to have the same fiber volume fraction. While this made the process of backing out the effective unidirectional stiffness and strength properties much simpler, in reality the subcells without the 0 degree fibers have a much lower fiber volume fraction due to the presence of the extra matrix material. In the course of this study, by including the fiber nesting the effects of the fiber volume ratio variation probably were cancelled out to some extent, which led to the relatively good correlations of the material stiffness. However, both the fiber nesting and fiber volume ratio assumptions could have contributed to the discrepancies in the strength predictions. For example, the subcells with the lower fiber volume ratio in reality should have a lower ultimate strength. The effects of including the fiber volume ratio variation will be investigated in future efforts, and means to account for this variation within the analytical model will be developed.

To further explore the capabilities of the model, the axial tension and transverse tension response of the T700/3502 material was also simulated. The experimental and simulated axial tension stress-strain curves are shown in Figure 22, and the transverse tension curves are shown in Figure 23. Table 10 shows a comparison between the experimental and computed moduli and strength for the axial tensile tests, and Table 11 shows a similar comparison for the transverse tensile tests. Note that once again numbers for the test data in the tables presented represent an average and one standard deviation for the tests conducted.
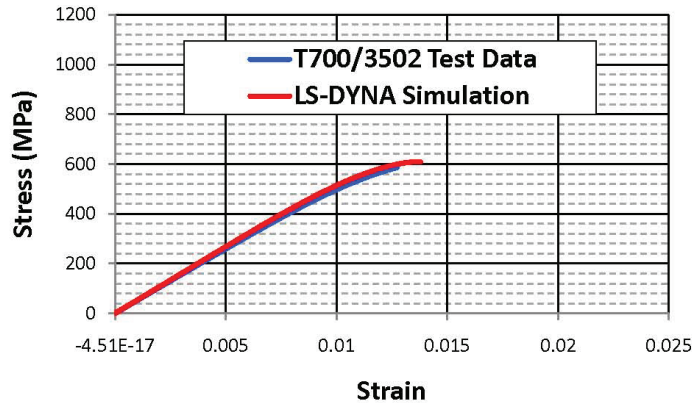
Figure 22.—Test versus simulation for T700 fiber/3502 resin axial tension material response.
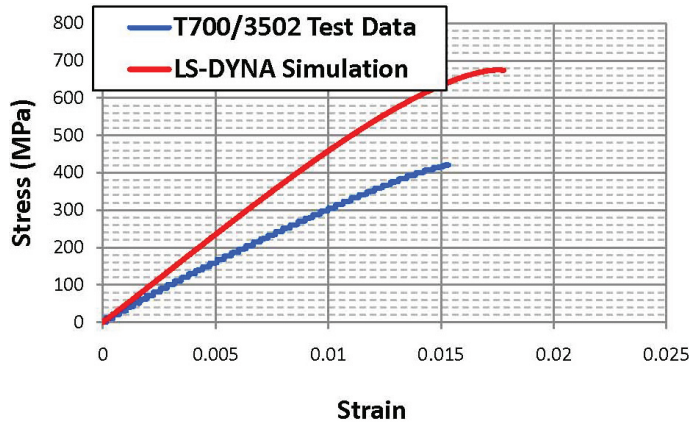

Figure 23.—Test versus simulation for T700 fiber/3502 resin transverse tension material response.

TABLE 10.—COMPARISONS BETWEEN T700 FIBER/3502 RESIN TEST AND LS-DYNA AXIAL TENSION DATA

	Axial tension modulus, GPa	Axial tension strength, MPa
Test	46.89±2.2	606.76±56.54
LS–DYNA	53.02	609.13
Error, percent	11.6	0.4

TABLE 11.—COMPARISONS BETWEEN T700 FIBER/3502 RESIN TEST AND LS-DYNA TRANSVERSE TENSION DATA

|	Transverse tension modulus, GPa	Transverse tension strength, MPa
Test	35.85±4.1	330.96±10.34
LS–DYNA	46.71	675.06
Error, percent	23	51

The reasonably good correlation between the experimental and simulated moduli for both the axial and transverse tension loading conditions, the close correlation of the axial tension strength and the overprediction of the transverse tension strength are similar to what was observed for the T700/PR520 material. The discussion and explanation of these results is therefore likely similar as to what was presented for the PR520 material. The model did capture the similarity in modulus, and the reduction in strength, in the T700/3502 material as compared to the T700/PR520 material. Furthermore, the slight nonlinearity observed in the axial tension tests for the T700/3502 material was captured by the model.

Impact Simulations

The composite materials presented in this research are primarily going to be used in impact situations, in which the impact resistance of these materials must be known and quantified. This section presents preliminary investigations which use the developed composite computer models for impact simulations for the detection and prediction of impact velocity thresholds and failure depictions. The material system which has been extensively investigated earlier was examined for the impact simulations, the T700 fiber/PR520 resin material system.

In the impact tests, which were conducted in the NASA Glenn Research Center Ballistic Impact Laboratory and which are described in detail in Reference 14, a single stage compressed gas gun was used to propel a soft projectile into 61 cm (24 in.) by 61 cm (24 in.) by 3.2 mm (0.125 in.) composite panels. The composite panel was held in a 5.1 cm (2 in.) wide steel picture frame fixture with 51 by 51 cm (20 in.) aperture. The projectile was a mixture of gelatin and phenolic microballoons. The composition was similar to that of projectiles commonly used to simulate bird strikes on aircraft. The molded projectile was a cylinder with a length of 12.7 cm (5 in.), a diameter of 7.0 cm (2.75 in.), and a nominal density of 0.96 g/cm^3. A soft projectile was used rather than a hard projectile because the objective was to induce a high strain energy density in the composite material before failure. Tests were performed over a range of impact velocities to determine the velocity for onset of damage, the growth of damage with increasing velocities, the penetration threshold, and the damage pattern induced by penetration. The penetration velocity depended on the material system, but velocities above 500 ft/s were common for the more impact resistant material systems. High speed cameras and an optical strain measurement system were used to obtain data such as out of plane displacement, strain in the vertical direction (approximately equal to material axial strain) and strain in the horizontal direction (approximately equal to material transverse strain).

Six T700S/PR520 panels were impacted using impact velocities ranging from 122 m/s (400 ft/s) to 230 m/s (756 ft/s). The lowest velocity impact produced no visible damage and the highest impact velocity completely penetrated the panel. The threshold velocity for penetration was between 191 m/s (627 ft/s) and 194 m/s (637 ft/s). A test performed at 194 m/s (637 ft/s) resulted in penetration of the panel by the projectile. Figure 24 shows a sequence of frames from the high speed video (along with simulation results which will be discussed later) showing first fiber failure, growth of the initial damage area, and finally crack initiation in the vertical direction leading to penetration by the projectile. Note that the vertical propagation of the crack for the panel tested at 194 m/s (637 ft/s) is not typical of most other material systems that have been tested. As discussed in Reference 14, more commonly the impacted panels show some crack propagation along the bias fiber directions, which is a more common mode of failure for these other material systems. To conduct simulations of the impact tests described above, the flat panels used for in the impact tests were modeled using a finite element mesh 0.6096 m (24 in.) wide, 0.6096 m (24 in.) tall and 0.3175 cm (0.125 in.) thick with 16320 shell elements. The finite element model of the panel is shown in Figure 25.
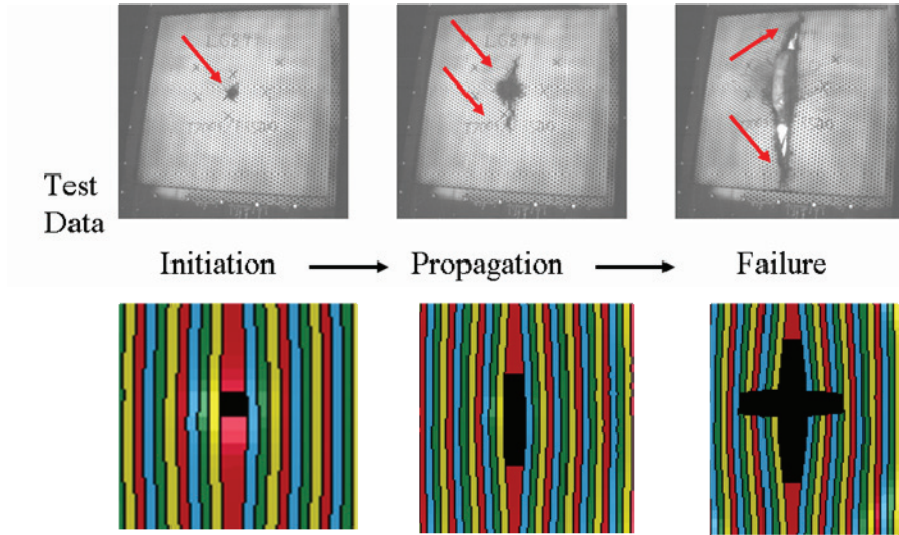
Simulation

Figure 24.—The progression of failure in the T700 fiber/PR520 resin material system at 194 m/sec as observed in impact tests (top) and predicted by numerical simulation (bottom) where initial fiber failure, crack initiation and crack propagation are shown.
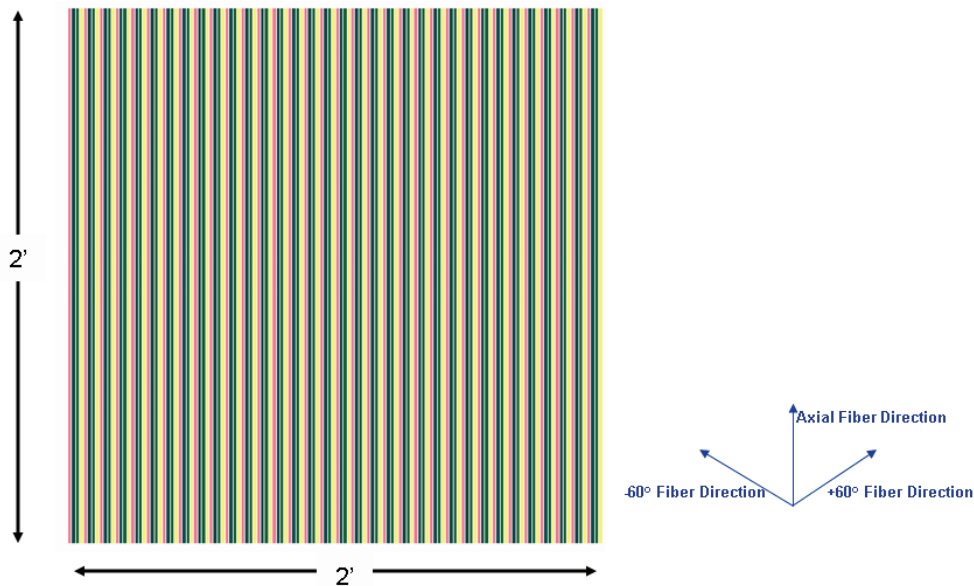

Figure 25.—Finite element impact composite model.

The alternating patterns of pink, blue, green, and yellow represent the four subcells used to simulate the composite braid geometry. The four sides of the panel were constrained in all three displacement and all three rotation directions. Because the gelatin is a low strength, low stiffness and high flow material, it was modeled as a fluid with a specified pressure-volume relation. The material equation of state relationship was also used for simulation of the shock wave at initial contact. To account for the extreme deformation of the gelatin during impact, the gelatin geometry was implemented into an Arbitrary Lagrangian Eularian (ALE) mesh which allowed the gelatin to flow freely and exhibit large deformations.

This model was able to simulate the large deformation of the projectile shown in Figure 14. Further details about the gelatin model can be found in (Ref. 8). The model parameters were adjusted in part by correlation with results of previous impact tests on composite panels. This is a limitation on the predictive capability of the current simulation method, and improved projectile models are being considered. The gelatin was modeled using 41040 solid elements.

Simulations were run for various impact velocities above and below the penetration threshold. The penetration threshold in the simulations was defined as the velocity at which any element completely failed, with all of the integration points failing. The model predicted penetration taking place at an impact velocity of 191 m/sec (627 ft/s), which agreed well with the experimentally determined velocity threshold of 194 m/sec (637 ft/s). For this case of impact penetration, the initiation and progression of damage was also compared to the experimental results. The experimental and predicted damage patterns are shown in Figure 24.

In the experiments the damage initiated in the middle of the panel and propagated in the vertical direction parallel to the axial fibers. The simulation captured the failure initiation and the initial propagation of damage. However, transverse cracks occurred later in the simulation. The damage pattern in the simulations is similar to that shown for a homogeneous material in Figure 9. This is probably caused by the assumption of constant fiber volume fraction in all subcells. This can best be explained by examining Figure 11. The constant fiber volume assumption artificially strengthens the bias fibers in subcells B and D. Because of the fiber angles within these subcells, the increased fiber strength would suppress crack propagation along the bias fiber direction and the axial direction to a greater extent than along the transverse direction. An initial set of parametric studies indicated that the model in its current form cannot simulate experiments in which cracks grow along bias fiber directions. In the simulations performed by Cheng (Fig. 10) it was possible to simulate crack growth in bias fiber directions by reducing the fiber volume fraction in subcells B and D and adjusting other model parameters. This suggests that it should be possible to better simulate crack propagation using the new model as the model is refined. If this can be achieved, the advantage of the new approach is that the fiber architecture in a multilayer laminate can be better represented and there is a clear methodology for obtaining material properties from experimental data and setting parameters (such as the stress limiting factors) to reflect actual material behavior. Although damage in the impact tests was not adequately simulated, preliminary results indicate that the simulations correlate well with the overall panel deformation.

Conclusions

The coordinated test/analysis method presented in the paper appears to be a promising approach for simulating ballistic impact of triaxial braid composite materials used for engine fan containment systems. The analysis method is computationally efficient and uses data directly measured on coupon specimens made with the triaxial braid material. Damage initiation and initial propagation of the crack during impact were simulated for the material system presented in this paper. Data used in the analysis was obtained using standard composite test methods augmented by full-field strain measurement. Several improvements are needed to make the simulation method more accurate and more capable of representing the wide range of failure modes that have been observed for different material systems. Continued work is needed to eliminate edge effects and ensure uniform deformation in the gage section of tensile test specimens. Data from tests that involve multiaxial loading, out of plane bending, and high strain rates would improve material characterization and provide data for better model validation. Methods to more accurately reflect the variations of local fiber volume fraction within the composite unit cell in the process of characterizing the analytical model need to be developed. Furthermore, methods to obtain more realistic estimates of the local fiber bundle stresses as a function of the global applied stress need to be investigated. These refined calculations will be used to provide more realistic values for the equivalent unidirectional composite strength properties used in the model. The simulation approach described in this paper should be a suitable framework for implementation of these improvements as the newer information becomes available.

References

1. Chou, T.W. and Ishikawa, T.: "Analysis and Modeling of Two-Dimensional Fabric Composites," in Textile Structural Composites, Composite Material Series, vol. 3, T.W. Chou and F.K. Ko, Eds., Elsevier Science Publishers B.V., Amsterdam, 1989, ch. 7, pp. 209–277.
2. Naik, N.K.; and Shembedkar, P.S., "Elastic Behavior of Woven Fabric Composites: I-Lamina Analysis," Journal of Composite Materials, vol. 26, pp. 2196–2225, 1992.
3. Pastore, C.M. and Gowayed, Y.A. A Self-Consistent Fabric Geometry Model: Modifications and Application of a Fabric Geometry Model to Predict the Elastic properties of Textile Composites. Journal of Composites Technology and Research vol. 16. no. 1, 1994.
4. Byun, Joon-Hyung. The analytical characterization of 2-D braided textile composites. Composites, Science, and Technology vol. 60, 705–716, 2000.
5. Tanov, R. and Tabiei, A. Computationally Efficient Micromechanical models for Woven Fabric Composite Elastic Moduli. Journal of Applied Mechanics, 68. 2001.
6. Bednarcyk, B.A.; "Modeling Woven Polymer Matrix Composites Using MAC/GMC," NASA/CR—2000-210370, 2000.
7. Roberts, G.D et al. Impact Testing and Analysis of Composites for Aircraft Engine Fan Cases. NASA TM 211493, 2002.
8. Cheng, Jingyun. Material Modeling of Strain Rate Dependent Polymer and 2D Triaxially Braided Composites. Ph.D. Dissertation, University of Akron, Akron, Ohio, 2006.
9. Livermore Software Technology Corporation. LS-DYNA Keyword Manual v 971. Livermore, CA, 2007.
10. ASTM D 3039, Standard Test Method for Tensile Properties of Polymer Matrix Composites, 2000.
11. ASTM D 3410, Standard Test method for Compressive Properties of Polymer Matrix Composite Materials With Unsupported Gage Section by Shear Loading, 2003.
12. ASTM D 5379, Standard Test Method for Shear properties of Composite Materials by the V-Notched Beam Method, 2005.
13. ASTM D 7078, Standard Test Method for Shear Properties of Composite Materials by V-Notched Rail Shear Method, 2005.
14. Roberts, G.D., et al. "Characterization of Triaxial Braided Composite Material Properties for Impact Simulation," American Helicopter Society Technical Conference.
15. Littell, J.D. "The Experimental and Analytical Characterization of the Macromechanical Response for Triaxial Braided Composite Materials," Doctor of Philosophy Dissertation, University of Akron, Akron, Ohio, 2008.
16. Matzenmiller, A. et al., A Constitutive Model for Anisotropic Damage in Fiber-Composites. Mechanics of Materials 20, 125–152. 1995.
17. Daniel, I.M. and Ishai, O.: Engineering Mechanics of Composite Materials Second Edition, Oxford University Press, New York, 2006.

REPORT DOCUMENTATION PAGE					*Form Approved* *OMB No. 0704-0188*
The public reporting burden for this collection of information is estimated to average 1 hour per response, including the time for reviewing instructions, searching existing data sources, gathering and maintaining the data needed, and completing and reviewing the collection of information. Send comments regarding this burden estimate or any other aspect of this collection of information, including suggestions for reducing this burden, to Department of Defense, Washington Headquarters Services, Directorate for Information Operations and Reports (0704-0188), 1215 Jefferson Davis Highway, Suite 1204, Arlington, VA 22202-4302. Respondents should be aware that notwithstanding any other provision of law, no person shall be subject to any penalty for failing to comply with a collection of information if it does not display a currently valid OMB control number. PLEASE DO NOT RETURN YOUR FORM TO THE ABOVE ADDRESS.					

1. REPORT DATE *(DD-MM-YYYY)* 01-03-2010	2. REPORT TYPE Technical Memorandum	3. DATES COVERED *(From - To)*

4. TITLE AND SUBTITLE Effect of Microscopic Damage Events on Static and Ballistic Impact Strength of Triaxial Braid Composites	5a. CONTRACT NUMBER
	5b. GRANT NUMBER
	5c. PROGRAM ELEMENT NUMBER
6. AUTHOR(S) Littell, Justin, D.; Binienda, Wieslaw, K.; Arnold, William, A.; Roberts, Gary, D.; Goldberg, Robert, K.	5d. PROJECT NUMBER
	5e. TASK NUMBER
	5f. WORK UNIT NUMBER WBS 698259.02.07.03.04.01

7. PERFORMING ORGANIZATION NAME(S) AND ADDRESS(ES) National Aeronautics and Space Administration John H. Glenn Research Center at Lewis Field Cleveland, Ohio 44135-3191	8. PERFORMING ORGANIZATION REPORT NUMBER E-17148

9. SPONSORING/MONITORING AGENCY NAME(S) AND ADDRESS(ES) National Aeronautics and Space Administration Washington, DC 20546-0001	10. SPONSORING/MONITOR'S ACRONYM(S) NASA
	11. SPONSORING/MONITORING REPORT NUMBER NASA/TM-2010-216095

12. DISTRIBUTION/AVAILABILITY STATEMENT Unclassified-Unlimited Subject Category: 24 Available electronically at http://gltrs.grc.nasa.gov This publication is available from the NASA Center for AeroSpace Information, 443-757-5802

13. SUPPLEMENTARY NOTES

14. ABSTRACT The reliability of impact simulations for aircraft components made with triaxial-braided carbon-fiber composites is currently limited by inadequate material property data and lack of validated material models for analysis. Methods to characterize the material properties used in the analytical models from a systematically obtained set of test data are also lacking. A macroscopic finite element based analytical model to analyze the impact response of these materials has been developed. The stiffness and strength properties utilized in the material model are obtained from a set of quasi-static in-plane tension, compression and shear coupon level tests. Full-field optical strain measurement techniques are applied in the testing, and the results are used to help in characterizing the model. The unit cell of the braided composite is modeled as a series of shell elements, where each element is modeled as a laminated composite. The braided architecture can thus be approximated within the analytical model. The transient dynamic finite element code LS-DYNA is utilized to conduct the finite element simulations, and an internal LS-DYNA constitutive model is utilized in the analysis. Methods to obtain the stiffness and strength properties required by the constitutive model from the available test data are developed. Simulations of quasi-static coupon tests and impact tests of a represented braided composite are conducted. Overall, the developed method shows promise, but improvements that are needed in test and analysis methods for better predictive capability are examined.

15. SUBJECT TERMS Composite materials; Braided composites; Graphite-epoxy composites; Composite structures; Impact tests; Load tests; Finite element method

16. SECURITY CLASSIFICATION OF:			17. LIMITATION OF ABSTRACT	18. NUMBER OF PAGES	19a. NAME OF RESPONSIBLE PERSON STI Help Desk (email:help@sti.nasa.gov)
a. REPORT U	b. ABSTRACT U	c. THIS PAGE U	UU	36	19b. TELEPHONE NUMBER *(include area code)* 443-757-5802

Standard Form 298 (Rev. 8-98)
Prescribed by ANSI Std. Z39-18